Humid phases on the southwestern Arabian Peninsula are consistent with the last two interglacials

Abi Stone [a,*], Robyn H. Inglis [b,1], Ian Candy [c], Diana Sahy [d], Anne-Lise Jourdan [e], Dan N. Barfod [f], Abdullah M. Alsharekh [g]

[a] *Geography Department, School of Environment, Education and Development, The University of Manchester, Oxford Road, Manchester, M13 9PL, UK*
[b] *Department of Archaeology, University of York, York, UK*
[c] *Centre for Quaternary Research, Department of Geography, Royal Holloway University of London, Egham, Surrey, UK*
[d] *British Geological Survey, Keyworth, NG12 5GG, Nottingham, UK*
[e] *University College London. Earth Sciences, 5 Gower Place, London, WC1E 6BS, UK*
[f] *NEIF Argon Isotope Laboratory, Scottish Universities Environmental Research Centre, East Kilbride, Scotland*
[g] *Department of Archaeology, College of Tourism & Archaeology, King Saud University, Riyadh, Saudi Arabia*

ARTICLE INFO

ABSTRACT

Past environmental and climatic conditions within the Arabian Peninsula are key to understanding the setting for hominin dispersal across the Saharo-Arabian dryland belt. The tufa deposits within the volcanic harrats on the southwest coast of Saudi Arabia fill a significant spatial gap in the distribution of palaeoenvironmental records on the west coast of the Arabian Peninsula adjacent to the Red Sea. In the catchment of Wadi Dabsa in the Harrat Al Birk, there are widespread fossil palustrine to shallow-lacustrine tufa deposits with fluvial elements. Several phases of tufa accumulation, separated by fluvial downcutting, are observable within these powerful palaeoenvironmental proxies. U–Th dating of targeted dense, banded tufa facies, yield ages that are stratigraphically consistent at the landscape scale, and indicate that tufa accumulation occurred during distinct humid phases broadly coeval with the last two warm interglacial Marine Isotope Stages (MIS 7 and MIS 5). For the first time this shows humid intervals in southwest Arabia coincident with the southern coast. There is a simlar pattern emerging further north in the Arabian Peninsula, The Sinai and Levant and further on into continental Europe. Furthermore, tufa $\delta^{18}O$ ranges from -14.6 to -1.9‰, covering a range similar to those reported for tufa from north African oasis sites and speleothems elsewhere on the Arabian Peninsula and The Levant. The lowest $\delta^{18}O$ values are derived from MIS 5e samples, a pattern in agreement with speleothems in Yemen and Oman, and consistent with an isotopic-enabled climate model simulation for this time slice. The $\delta^{13}C$ and Sr isotopic compositions of dated tufa samples indicate deposition from shallow-circulating meteoric water, with no geothermal influence. This, along with the $\delta^{18}O$ values, suggest a freshwater supply that was a potable water source in this landscape. The $\delta^{13}C$ signatures at Wadi Dabsa are more negative than for parts of north Africa, suggesting Wadi Dabsa may have experienced comparatively higher biomass, thicker soils and wetter conditions with lower evaporative losses. This new record of tufa deposition during the middle and late Pleistocene, suggests for the first time that the west coast of Arabia experienced a similar history of humid phases over the past 250 ka as southern Arabia and the Nefud in the northern interior. These regional changes in hydroclimatic regime occur at timescales coincident with hominin dispersals.

1. Introduction

The Arabian Peninsula is a key region for understanding the dispersal of hominins from Africa into the Middle East and onward, as reflected in field-based research (e.g. Petraglia, 2003; Bailey, 2009; Armitage et al., 2011; Bailey et al., 2015; Breeze et al., 2016; Groucutt et al., 2015; Jennings et al., 2015; Bae et al., 2017; Crassard and Hilbert, 2013; Clark-Balzan et al., 2018; Groucutt et al., 2018; Parton et al., 2018;

Scerri et al., 2018; Crassard et al., 2019; Inglis et al., 2019; Nicholson et al., 2020; Stewart et al., 2020; Groucutt et al., 2021) and in model simulations (e.g. Jennings et al., 2015; Kutzbach et al., 2020). The current semi-arid and arid conditions of the Saharo-Arabian belt present harsh, inhospitable environments. Consequently, it is now widely accepted that hominin dispersals were facilitated by the episodic occurrence of humid phases when the now desert-like conditions were replaced by savanna ecosystems, containing numerous and persistent bodies of fresh surface water. Past humid phases, within the present-day dryland Saharo-Arabian belt, are commonly referred to as 'pluvial' conditions, 'greenings' or 'green corridors' (e.g. Kutzbach, 1981; Burns et al., 2001; Drake et al., 2011; Fleitmann et al., 2011; Rosenberg et al., 2011, 2013; Larrasoaña et al., 2013; Jennings et al., 2015; Breeze et al., 2016; Timmerman and Friedrich, 2016; El-Shenawy et al., 2018; Roberts et al., 2018; Nicholson et al., 2020). However, the spatial distribution of current palaeoenvironmental records within the Arabian Peninsula upon which these interpretations are based is highly uneven. The west of the Arabian Peninsula on the Red Sea Coast has a striking lack of published palaeoenvironmental records (for example, as highlighted in a recent palaeoenvironmental synthesis of the last 20 ka in the Arabian Peninsula by Woor et al. (2022)). This study addresses the call by Nicholson et al. (2021, p1) for "further studies" being needed "to understand spatio-temporal difference in human-environment interactions in (this) climatically variable region." In doing so, we explore whether this region responds to climatic changes in a manner that is consistent or distinct from other parts of the Arabian Peninsula.

An improved spatial coverage of palaeoenvironmental records across the Saharo-Arabian belt is important for understanding what drove past humid phases, including precession-paced insolation maxima in the Northern Hemisphere, which strengthens the global monsoon and extends its spatial coverage (e.g. Kutzbach, 1981; Kutzbach et al., 2020). The speleothem growth records from Mukalla and Hoti Caves indicate that all 21 humid intervals of the last 1.1 million years across the southern and south-eastern coast of the Arabian Peninsula occurred during the peaks of interglacials, or in the case of MIS 27, 15, 13, 9, 7 and 5 during warm sub-stages of these interglacials (Nicholson et al., 2020). The interpretation is that global glacial conditions dampen the influence of the monsoon over the southern Arabian Peninsula (Fleitmann et al., 2011; Nicholson et al., 2020; Nicholson et al., 2021). Furthermore, the stable oxygen isotopic signatures (δ^{18}O) for speleothem carbonate during different growth intervals over the last 350 ka suggest that MIS 5e received the greatest/highest intensity precipitation followed by MIS 7, then later in MIS 5, and MIS 9 (Fleitmann et al., 2011). In contrast, the chronological control for lacustrine phases in the Nefud, northern Arabia, are not tightly constrained to interglacials, with ages in late MIS 6 at Khall Amayshan 4 (KAM 4) (Groucutt et al., 2021), in MIS 4 at Al Marrat (Jennings et al., 2015), and in early MIS 3 at Jubbah (Petraglia et al., 2012; Parton et al., 2018). The fluvial outwash sediments near Al-Quwaiyah in the centre also record fluvial activity during MIS 3 (McLaren et al., 2009), as do alluvial fan systems in the eastern United Arab Emirates UAE, at Remah (Farrant et al., 2012) and at Al Sibetah (Parton et al., 2015), and the lacustrine record at Mundafan and Khujaymah in the western part of the southern Rub' al-Kali (Rosenberg et al., 2011). In Egypt, phases of tufa carbonate deposition occurred during glacial phases, as well as interglacials (see Kele et al. (2021) for an overview). Similarly, the humid periods in the Negev Desert, constrained from speleothem growth records, are not strictly aligned with interglacials: the first starts in late MIS 10 and extends into MIS 9; the second is contained within MIS 9; the third is contained within MIS 7 and the fourth starts in late MIS 6, extending into MIS 5 (e.g. Vaks et al., 2010). West of the Red Sea in the Eastern and Western Deserts of Egypt, the δ^{18}O signatures within tufa have been interpreted as indicating either a westerly Atlantic Ocean precipitation source or an Indian Ocean rainfall source for Egyptian aquifer recharge (Smith et al., 2004), with Kele et al. (2021) and Rogerson et al. (2019) suggesting a Mediterranean source is also important. Furthermore, Kele et al. (2021) hypothesise a

non-monsoonal rainfall source for the glacial-age tufa in Egypt, suggesting that tufa activity (deposition) and rainfall during glacial periods were driven by the presence of an Indian Ocean Warm pool during lower sea levels within glacial periods. We require better spatial coverage of palaeoenvironmental records to further interrogate these patterns of palaeoclimatic change.

There is, therefore, a strong imperative to reconstruct humidity histories at a wider range of sites, using available palaeoenvironmental proxies, including tufa. Until now, information about tufa in Saudi Arabia and Oman has been limited to their location and textural characteristics (Whitton et al., 1986; Kabesh and Abdel-Motelib, 2014; Khalaf, 2017), with some detailed petrology and geochemical composition (e.g. Stone et al., 2022), but no age control. This study aims to fill a key gap in the spatial syntheses for the Arabian Peninsula by reconstructing the timing of humid phases in the south of the western coastal plain of Saudi Arabia. Our palaeoenvironmental proxy is fossil tufa carbonates laid down at Wadi Dabsa within the Harrat Al Birk Volcanic fields (Fig. 1). We use paired U–Th and δ^{18}O analysis on the same depositional units, which allows us to provide a temporal record of shifts in δ^{18}O, and from this make inferences into the precipitation regime, including a comparison with existing records from other carbonates (tufa and speleothem) in the Saharo-Arabian belt. There are lithic artifacts at Wadi Dabsa and nearby sites (e.g. Foulds et al., 2017; Inglis et al., 2019). This tufa system has already been demonstrated to have been deposited in a cool, freshwater environment, from their ^{87}Sr/^{86}Sr isotopic ratios and the range of the stable carbon isotopic (δ^{13}C) signatures (Stone et al., 2022). Tufa are biomediated deposits, formed in terrestrial freshwater environments, involving shallow water-rock interactions and carbon dioxide derived from the terrestrial biosphere (Ford and Pedley, 1996). Tufa are a sedimentary response to their surrounding hydrogeological system, and as such are not necessarily straightforward, responding to: (i) an increase in water availability, (ii) changes to vegetation amounts and types, (iii) variations in soil development, and (iv) other controls on the solution of calcium carbonate within the water, such as temperature (e.g. Ford and Pedley, 1996; Brasier et al., 2011; Capezzouli et al., 2014). Nonetheless, in arid and semi-arid regions, which lack perennial standing water, the presence of fossil tufa indicates wetter conditions and/or a higher groundwater table. Furthermore, the stratigraphic organisation of different tufa facies can record regime shifts in the surface water environment (e.g. Viles et al. (2007) and Stone et al. (2010) in the Naukluft Mountains of Namibia and Stone et al. (2022) here at Wadi Dabsa). In addition to U–Th dated phases of tufa accumulation, their stable isotopic composition can be used to characterise the climatic conditions under which they formed (see overview by Capezzouli et al., 2014). In this paper we discuss both the timing of tufa formation and the preserved palaeoenvironmental information in order to understand the palaeoclimatic history of this locality across the Middle and Late Pleistocene. We conclude by discussing the implications of these results for the dispersal of early humans and changes in atmospheric circulation in this important region.

2. Setting

The present climate of the Arabian Peninsula is influenced by four main atmospheric circulation systems: 1) the seasonally-shifting global monsoon circulation system (Wang et al., 2017), including the Indian Summer Monsoon (ISM) and African Summer Monsoon (ASM) components; 2) the summer north-westerly Shamal wind, driven by the steep pressure gradient between the semi-permanent high pressure over northern Arabian and low pressure in boreal summer over northwest India through to Iran (Yu et al., 2016); 3) mid-latitude westerlies, bringing winter frontal rain (Rodwell and Hoskins, 1996; Tyrlis et al., 2013) and 4) the Red Sea Trough synoptic system, which brings infrequent extreme precipitation in the autumn (de Vries et al., 2013). During the boreal summer the InterTropical Convergence Zone (ITCZ) moves further north bringing increased precipitation to the southern part of the
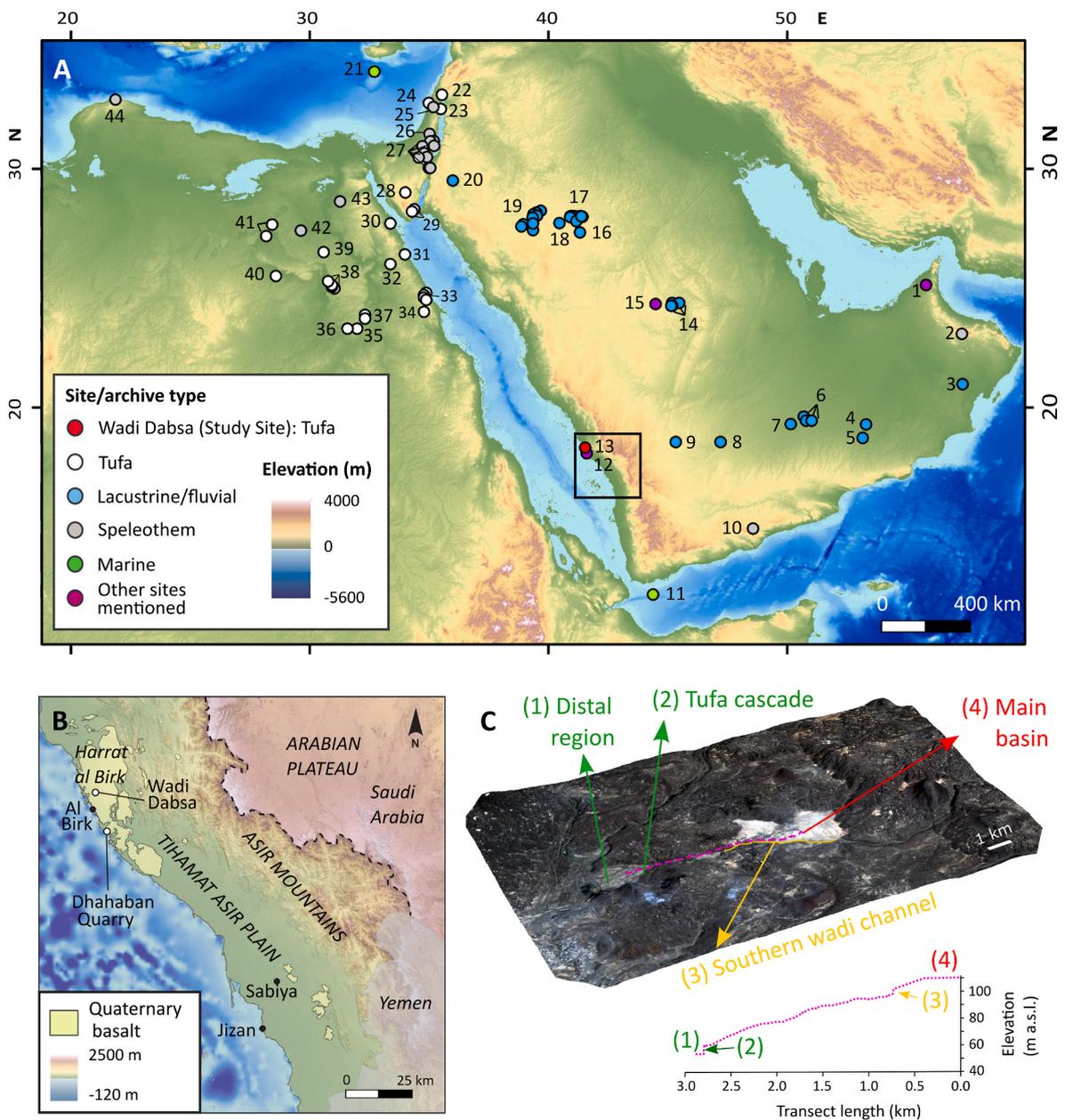
Fig. 1. (A) Location map showing sites of palaeoenvironmental records for the late Pleistocene on the Arabian Peninsula, the Levant and Palestine/Israel, and into western North Africa, as well as other sites mentioned in the text, alongside the location of the Wadi Dabsa study site, noting that the Tadrart Acacus (tufa site) in Libya is out of view, further west. See Supp. Info 1 for corresponding site names. Topographic and bathymetric data from GEBCO Compilation Group, 2022 , (B) Location of the Harrat al Birk on the Tihamat Asir Plain on south-western Saudi Arabia (adapted from Inglis et al., 2019), (C) Dabsa Basin, indicating the four key locations of investigated tufa (surface of the main basin, southern wadi channel, tufa cascade and distal region), on an ASTER 30 m GEDM, with 3x vertical exaggeration using Pleiadas 1 Multispectral true colour scheme) (adapted from Inglis et al. (2019). See Supp. Info. 2 for detailed information about field locations of each sample at Wadi Dabsa and photographs.

peninsula. There are accompanying shifts in high and low-pressure cells, including the southern-hemisphere Mascarene High (Ohishi et al., 2015) and its influence on cross equatorial jet streams with anticyclonic flow in boreal summer that can reach the peninsula (Findlater, 1969; Krishna-murti and Bhalme, 1976). Northern Arabia, the Levant and the Sinai Peninsula receive rain in boreal winter from cyclones in the mid-latitude westerlies (Black, 2011), whilst the central regions receive infrequent but intense precipitation in boreal autumn derived from the Red Sea Trough (de Vries et al., 2013).

Wadi Dabsa (18.30°N, 41.57°E) is on the western coastal plain of southwest Saudi Arabia. The present climate of this region is arid, with nearby Jeddah (21.45°N, 39.23°E) receiving 51 mm/y of precipitation (Hasanean and Almazroui, 2015), mostly during a wet season from

November to April. Mean average annual temperatures are ~30 °C, using records for Jizan (16.90°N, 42.56°E) (Sen and Al-Suba'I, 2002). This part of the Red Sea coast is a region where the four main atmospheric climatic systems overlap (Rohling et al., 2013), which makes Wadi Dabsa a valuable location to explore the existing hypotheses for the receipt of moisture over the Saharo-Arabian belt during the humid intervals of the past few hundred thousand years. These hypothesised sources include: moisture from the Atlantic Ocean (westerly rainfall systems); moisture from the Indian Ocean (eastward moving monsoonal rainfall systems) (e.g. Smith et al., 2004); a non-monsoonal easterly moisture source linked to the presence of a glacial-period Indian Ocean Warm Pool (Kele et al., 2021) and moisture from the Mediterranean Sea (Kele et al., 2021; Rogerson et al., 2019).

The geomorphic setting of Wadi Dabsa is a former, non-thermal, palustrine to shallow-lacustrine system with fluvial elements within the volcanic Harrat Al Birk (Stone et al., 2022) (Fig. 1). Table 1 gives a schematic overview of the four key positions where tufa is found in the landscape (labelled on Fig. 1C), alongside a summary description of stratigraphical units in the two locations they are visible in the field. A more detailed description of tufa facies types and depositional environments is given in Stone et al. (2022). There is a 1.6 km long (east--west oriented) main basin that is divided into two parts by a northeast-southwest orientated central Wadi, and ~50% of the surface of this basin has tufa exposed at the surface (Fig. 1C; Supp. Info. Fig. S2.1B). The eastern part has a higher elevation (dominantly 110–115 m a.s.l. with a maximum of 123 m a.s.l. at the eastern edge) than the western part (90–109 m a.s.l, which decreases towards the southwest). The elevation of the central wadi channel decreases from northeast to southwest (~115–~98 m a.s.l.), at which point it joins a wadi running along the southern edge of the basin (Fig. 1C, Supp. Info 2.1). Further downstream the southern wadi has a ~1 km reach constrained by local bedrock (basaltic flows), before opening out onto a distal region, with a rhomboid shape that is controlled by the morphology of the surrounding basalt lobes (Fig. 1C, Supp. Info. S2.1). This distal region slopes toward the west, with elevation reducing from ~45 to 35 m a.s.l.. At the break of slope where the wadi emerges onto the distal region, 6 m high tufa cascades crop out and a stratigraphic record is preserved (Supp. Info. Fig. S2.1, S2.4). The distal region contains multiple shallow (<1 m deep) channels and surface exposures of *in situ* tufa as well as eroded boulders of tufa (Supp. Info. Fig. S2.5).

The tufa found *in situ* across the surface of the main basin is heavily eroded in places, including reworked clasts of tufa and basalt clasts (see Supp. Info. Fig. S2.2). The tufa facies types observed are diverse and using the descriptive scheme of Arenas-Abad et al. (2010), these include: phytoherm (Lbr); phytoherm tufa of stems (Lst); stromatolitic (Ls), phytoclastic (LpH); and bioclastic-charophytic (Lb-ch) (Supp. Info. 2, Fig. S2.2). This mosaic of facies types is interpreted by Stone et al. (2022) to be indicative of a palustrine to shallow-lacustrine system, containing fluvial channels and drier islands. The topography between the eastern basin and central wadi provides small breaks of slope (10s of cm) over which tufa barrages formed in the past (Supp. Info. Fig. S2.2I-K). Here there is a series of six fossil tufa barrages, with individual heights varying from 10 to 30 cm, convex size profiles and flat tops. We hypothesise that the mosaic of tufa facies exposed at the surface of the basin are broadly coeval, and younger than the units exposed at depth in the incised wadi channels.

The northern bank of the southern wadi reveals ~3 m exposure of tufa (at 18°18′23.50″ N, 41°33′40.10′′E), which contains four broad depositional units (Table 1; Supp. Info. Fig. S2.3). The base (unit 3i) is a matrix-supported conglomerate (~0.6 m thick), which indicates a phase of high-energy fluvial flow, followed by lower-energy flow during which the matrix is cemented by precipitation of tufa (Stone et al., 2022). Unit 3ii is a laterally discontinuous rudstone tufa (LI/Lph) (maximum of 20 cm thick) containing gravel clasts, indicative of lower fluvial energy than the boulder-rich unit below. Above this there is a ~0.6 m unit of bryophyte (Lbr) facies, coated with dense, banded tufa (5–10 cm thick) (grouped as unit 3iii). The final unit (3iv) contains lobes of Lst/Lbr tufa without clasts, covering a thickness of 1.2 m.

The ~6 m high tufa cascade that outcrops at the break of slope near to the neck of the distal region of the landscape system offers another insight into the tufa stratigraphy (Supp. Info. Fig. S2.4). Viewed from the ground, as it was unsafe to climb during our short field visit to study in detail, we define four broad units. Unit 2i is a tufa-cemented conglomerate, again indicating a shift from high-energy fluvial flow that moved the bedload, to low-energy flow, during which the tufa precipitated. Unit 2ii is a horizontally discontinuous rudstone layer containing smaller clasts (gravels), indicating a lower energy environment than the unit below. Unit 2iii contains repeated layers of phytoherm tufa, characteristics of a cascade, before another tufa-cemented conglomerate unit (2iv) in a discrete former-fluvial channel that has eroded into the barrage. The uppermost unit (2v) contains repeated lobes of phytoherm

Table 1

Locations of tufa in the field across their position in the landscape, giving broad elevation ranges, summary of stratigraphy where observed, and cross-referencing the site number where tufa was extracted in the field for analysis.

	Position in the landscape			
	(1) Distal region	(2) Fossil tufa cascade outcrop where wadi emerges onto distal region	(3) Southern wadi channel exposure	(4) Main basin
Stratigraphic units observed in field (and hypothesised correspondence for the two locations with exposed stratigraphy)	Only surface outcrops are visible*	(2v) Phytoherm tufa (Lst/Lbr), variable thickness (max ~2 m).	(3iv) Phytoherm tufa (Lst/Lbr), variable thickness (max 1.2 m). (3iii) Phytoherm tufa (Lbr) ~0.6 m thick, overhanging the channel, coated in dense, banded tufa (0.05–0.10 m thick). (3ii) Rudstone tufa (Li/Lph), with gravel clasts, laterally discontinuous (max thickness 0.2 m). (3i) Tufa cemented, matrix-supported conglomerate with cobble and boulder sized clasts (max thickness 0.6 m).	Only surface outcrops are visible*
		(2iv) Tufa-cemented cobbles-to-boulders (G#2), in discrete location (perhaps a channel). (2iii) Phytoherm tufa (Lst/Lbr), thickness (max 3 m). (2ii) Repeating layers of rudstone tufa (Lph), which wedge out to unit 2iii above (max 1 m). (2i) Tufa-cemented conglomerate (G#1) (max thickness 0.5 m).		
Elevation range	35–45 m a.s.l.	45–51 m a.s.l.	97–100 m a.s.l.	E-portion, 115–123 m a.s.l. W-portion 90–109 m a.sl.,
Site number [WD T$_n$] with corresponding stratigraphical location	WD T3: exposed at the surface	WD T4: unit 2iii (1.5 m from base)	WD T5, T6: dense coating of unit 3iii (1.2 m from base)	WD T0, T10, T12, T13: exposed at the surface in locale of lithic artifact recording grids, WD T8: exposed at the surface close to southern wadi and WD T7, T11: fossil tufa barrages.

tufa. We hypothesise that unit 2iv (conglomerate) might correspond to unit 3i (conglomerate) in the southern wadi channel from the positions below the surface (hence the offset in Table 1).

The surface of the distal region contains *in situ* tufa, mostly undulating sheets of phytoherm facies (both LBr and Lst), with some regions with bioclastic charophyte facies (Lb-ch) (Supp. Info. Fig.S2.5). This is less complicated than the mosaic of facies types on the surface of the main basin, and this distal part of the system seems to have been a palustrine-to-fluvial system. There are eroded, remobilised clasts of tufa, alongside cobble-to-boulder sized basalt clasts. The *in situ* tufa on this surface is hypothesised to be coeval with that on the surface of the main basin, despite the difference in elevation (Table 1).

3. Sampling design and methods

Despite the widespread presence of tufa in this landscape, not all facies types are suitable for isotopic analysis or U–Th dating, owing to their highly porous nature and/or the amount of detritus they contain. For this reason, only dense, banded facies were targeted for analysis back in the laboratory, from a total of 12 sites across the landscape. The position of these sites is related to the stratigraphy observed across the four parts of the landscape in the final row of Table 1. Supp. Info. 2. depicts the sites on a map (Fig. S2.1), provides photographs of the four key positions in the land-system where tufa is found (Figs. S2.2 to S2.5), provides photographs of the stratigraphical sequences of units observed at positions 2 and 3 (Fig. S2.4, Fig. S2.5), and provides photographs of locations where tufa was extracted (Fig. S2.6).

Considering these from oldest (lowest unit in the landscape following the law of superposition) to youngest, the first site is WD T4, which is the tufa cascade (Supp. Info. Fig.S2.4). Here a vug-fill (flowstone-style) tufa facies was extracted (Supp. Info. Fig.S2.6L) from unit 2iii at a height of 1.5 m above the base of the cascade. Next, are neighbouring sites WD T5 and T6, located in the northern bank of the southern wadi channel (Supp. Info. Fig.S2.3), where tufa was extracted from unit 3iii at a height of 1.2 m from the wadi channel (Supp. Info. Fig.S2.6I,J). All other sites involved the extraction of a piece of tufa, exposed at the land surface, and are hypothesised to be broadly coeval. WD T3 is a site on the rhombus-shaped distal area (Supp. Info. Fig.S2.6K), whilst WD T0,10,12,13,14 (Supp. Info. Fig.S2.6A-E) are clustered on the surface of the eastern part of the main basin in the locale of the lithic artifact survey undertaken by Inglis et al. (2019) (Supp. Info. Fig. S2.1F). Site WD T8 is located 350 m southwest of the artifact recording grids (Supp. Info. Fig. S2.1E), with Fig.S2.6F showing the surface from which tufa was extracted and the tufa in hand-section. WD T7 and T11 were extracted from the fossil tufa barrages (Supp. Info. Fig.S2.6G,H), which are exposed at the surface on the slope between the eastern part of the main basin and the central wadi (Supp. Info. Fig.S2.2I-K). Tufa extracted from each site was sliced and thin sections were prepared at Royal Holloway University of London, which were used to guide the locations for micro-drilling for targeted U–Th dating and stable isotopic analysis, within dense, low-detrital concentration bands, or layers, within the tufa.

57 U–Th dating analyses were undertaken across the 12 pieces of dense, banded tufa extracted from the 12 field sites. To avoid confusion with stratigraphic units at the scale of exposures in the field (the units within Table 1) we use the notation band/layer to depict the small-scale (mm to cm) sedimentary layers within the extracted pieces of tufa. Supp. Info. 3 labels the bands/layers of each piece of tufa (with the exception of the piece at site WD T3 which does not contain bands/layers) and indicates the positions along these bands/layers that were micro-drilled (sampled) to extract material for analysis. With one exception every band/layer was micro-drilled in a minimum of 3 locations, to provide sub-samples (or multiple analyses) of that particular band/layer for U–Th and stable isotopic analysis. Samples (micro-drilled material) were analysed at the National Environmental Isotope Facility at the British Geological Survey, following the protocol outlined by Rowe et al.

(2020). In summary, samples weighing 10–100 mg were spiked with a ^{229}Th–^{236}U tracer, and U and Th were separated and purified through ion chromatography. U and Th fractions were analysed on Thermo Fischer Neptune Plus multi-collector ICP-MS using CRM112a and IRMM3636 uranium reference materials and an in-house ^{229}Th–^{230}Th–^{232}Th standard to monitor mass bias and detector performance. Local sediment and basalt were also micro-drilled to extract material to dissolve in a concentrated HF and HNO$_3$ mixture, and were then processed in a manner similar to the tufa samples, to gain additional data to aid age interpretation.

66 stable isotope analysis across the 12 pieces of tufa (2–3 subsamples per band/layer within a piece) (Supp. Info. 3 shows microdrilled locations), were undertaken. ~300 µg of carbonate was loaded into Exetainer® borosilicate vials, acidied with 0.1 ml of 100% phosphoric acid, with the released CO$_2$ gas passed through a Nafion® drying tube and into a Thermo Delta Plus XP mass spectrometer attached to a Thermo Gas Bench II at the Bloomsbury Environmental Isotope Facility at University College London.

Having replicate age control and stable isotope data for the same bands/layers within our targeted tufa material is critical, particularly to facilitate a robust palaeoclimatic interpretation of the stable oxygen isotopic values. In the existing published data for tufa across the Saharo-Arabian belt, the lack of ages for many of the stable oxygen isotope datasets has precluded their use in quantitative palaeoclimate reconstruction.

4. Results

The two main concerns in interpreting U–Th age data from the Wadi Dabsa tufa are the presence of initial ^{230}Th carried by detrital silicate minerals and possible open system behaviour in the form of U loss over time. (^{230}Th/^{232}Th) values in our samples range between 2 and 105 (Table 2), which makes it necessary to choose a threshold value below which we consider the impact of our initial ^{230}Th correction to be too high to confidently interpret age data. (^{230}Th/^{232}Th) > 20 has been suggested as an acceptable threshold in high-precision U–Th dating of speleothems for palaeoclimate applications (Hellstrom, 2006), and 29 of our analyses fall within this category, allowing us to consider data from samples WD T3,4,5, 7,8,10 and 11 as potentially reliable with respect to the efficacy of our initial ^{230}Th correction (Table 2). Arbitrarily choosing a higher threshold, e.g. (^{230}Th/^{232}Th) > 40 would rule out all data from WD T5 and 11, but this would not affect the conclusions of our study. It is worth noting that the aim of the U–Th dating carried out as part of this study is not the development of a high-precision and high-resolution palaeoclimate reconstruction based on the Wadi Dabsa tufa. Instead, the goal is simply to assign tufa growth to a particular marine isotope stage (MIS). With this in mind, we would argue that a lower threshold of (^{230}Th/^{232}Th) > 10 may be acceptable, which would allow us to also consider dates from tufa extracted at sites WD T0, 6, and 14 within our interpretation (Table 2).

Post-depositional alteration is a common problem in tufa U–Th dating (e.g. Garnett et al., 2004) and cannot be entirely ruled out in this case. Indeed, our initial sub-sampling strategy focused on an isochron approach to mitigate the impact of detrital silicates on U–Th isotope composition, but we abandoned this approach because: (a) many of the subsamples turned out to have favourable (^{230}Th/^{232}Th) values, and (b) scatter in excess of the analytical uncertainties in sub-samples from the same tufa made interpretation difficult. This scatter could be due to age variation between the sub-samples, variations in detrital U–Th isotope composition and/or post depositional U loss/gain affecting sub-sampled tufa locations in a random manner. Thin section observations provide additional information about: (i) the cements types (micrite or microspar), coupled with carbonate mineralogical composition data from XRD analysis; (ii) observed detrital particles (and their amount and size), along with composition data (XRD), and (iii) porosity estimates. These data are summarised in Table 2 alongside the accepted and rejected

Table 2

U–Th analysis (left-hand side) and stable isotope analysis (right-hand side), ordered according to their stratigraphic position across the landscape system (oldest to youngest) (see Table 1). For the U–Th analyses (columns 3 to 9), underlined samples show detrital contamination below a lower cut-off. The middle columns give thin section observations of cement types and chemical composition indicated from XRD analysis (reported in Stone al.(2022)), of detritus amounts, and of porosity. oxygen and carbon stable isotopic data (final three columns) with sample IDs.Column 1 (site)refers to the location at which the piece of tufa was extracted (see Supp. Info. 2). Column 2 (band/layer) refers to the mm-to-cm layers observed within the pieces of extracted densely-cemented tufa (with the exception of WD T3), and the letters cross-reference with labelling used in Supp. Info. 3. Column 3 (U–Th dating ID), depicts the material extracted via micro-drill for U–Th, arranged by row to show which band/layer they correspond with, and column 13 (Stable-isotope sample ID) depicts the material extracted via micro-drill for stable isotope analysis. There are multiple analysis (or sub-samples) for each of the bands/layers observed. Along a row it is possible to trace corresponding age-control and isotopic composition for observed bands/layers (see. Supp. Info. 3 for labelled photographs of the micro-drilled locations).

Site	Band/layer	U–Th dating ID	^{238}U (ppm)	^{232}Th (ppm)	(^{230}Th/^{232}Th)	Initial (^{234}U/^{238}U)	Detrital corrected (bulk crust) age (ka) (2σ)	Comments	Cement types	Detritus Amount & composition	Sa	Si	C	Porosity	Stable isotope sample ID	δ^{18}O	δ^{13}C
Unit 2iii in the tufa cascaderowhead																	
WD T4	B	1	0.14	0.09	5.8	1.64 ± 0.12	222.71 ± 10.70	DC (vp), Reject	mc lams, some m-s (o-g), (94% CaCO$_3$, 6% Mg CaCO$_3$)	<1% Q		•	•	1–2% Pores <0.1 mm	WD T4 i	−9.3	−10.0
	B	2	0.11	0.01	32.0	1.73 ± 0.02	195.38 ± 4.71	DC (p), Accept(1)							WDT 4 ii	−9.9	−10.2
	B	3	0.11	0.01	35.5	1.65 ± 0.02	190.35 ± 4.74	DC (p), Accept(1)							WDT 4 iii	−9.9	−10.3
	B	4	0.12	0.01	37.7	1.72 ± 0.02	232.88 ± 5.87	DC (p), Accept(1)									
	B	5	0.12	0.01	53.7	1.66 ± 0.01	216.35 ± 4.65	DC (p), Accept(1)									
	B	6	0.12	0.01	56.2	1.65 ± 0.01	208.82 ± 4.69	DC (p), Accept(1)									
	C	ND	ND	ND	ND	ND	ND	ND	mc, m-s (o-g), stain (p) (94% CaCO$_3$, 6% Mg CaCO$_3$) Dolomite	<1% Q, muscovite		•	•	10–30%	WDT 4 iv	−8.1	−10.2
	C	ND	ND	ND	ND	ND	ND	ND							WDT 4 v	−8.3	−10.1
	C	ND	ND	ND	ND	ND	ND	ND							WDT 4 vi	−8.3	−10.1
	Average of 5 accepted layer B samples							**211.1 ± 7.6**									
Unit 3iii in the bank of the southern wadirowhead																	
WD T5	A	ND	ND	ND	ND	ND	ND	ND	ND	1%		•	•	10–20%	WD T5 iv	−9.2	−7.5
	A	ND	ND	ND	ND	ND	ND	ND		ND					WD T5 v	−8.6	−7.6
	A	ND	ND	ND	ND	ND	ND	ND		ND					WD T5 vi	−9.2	−7.9
	D	1	0.20	0.03	22.57	1.73 ± 0.03	135.48 ± 2.05	DC (p), Accept(1)	mc, m-s (o-g), stain (m) & fil. (94% CaCO$_3$, 6% Mg CaCO$_3$)	1% Q		•	•	20–30%	WD T5 i	−8.6	−7.5
	D	2	0.21	0.03	21.51	1.68 ± 0.03	124.54 ± 2.26	DC (p), Accept(1)							WD T5 ii	−9.2	−7.9
	D	3	0.21	0.03	20.11	1.70 ± 0.03	125.25 ± 2.27	DC (p), Accept(1)							WD T5 iii	−9.0	−7.8
	Average (all samples accepted)							**128.4 ± 3.1**									
WD T6	NA	1	0.18	0.06	10.21	1.81 ± 0.06	136.27 ± 4.51	DC (vp), Accept(2)	mc, m-s (o-g), stain (m) & fil. (94% CaCO$_3$, 6% Mg CaCO$_3$)	1% Q		•		5–10%	WD T6 i	−14.6	−7.9
	NA	2	0.18	0.07	10.09	1.80 ± 0.07	135.04 ± 5.18	DC (vp), Accept(2)							WD T6 ii	−9.4	−7.7
	NA	3	0.20	0.09	7.48	1.83 ± 0.09	127.98 ± 6.19	DC (vp), reject							WD T6 iii	−12.8	−7.7
	Average of 2 accepted samples							**135.66 ± 6.9**									
Surface of main basinrowhead																	
WD T0	B	1	0.27	0.07	9.56	1.65 ± 0.05	82.85 ± 3.75	DC (vp), Reject	mc, m-s (100% CaCO$_3$)	1% Q	•			1%	WD T0 i	−4.8	−9.5
	B	2	0.31	0.18	4.11	1.61 ± 0.10	67.82 ± 8.75	DC (p), Reject							WD T0 ii	−4.1	−9.2

Table 2 (*continued*)

Site	Band/layer	U–Th dating ID	^{238}U (ppm)	^{232}Th (ppm)	(^{230}Th/^{232}Th)	Initial (^{234}U/^{238}U)	Detrital corrected (bulk crust) age (ka) (2σ)	Comments	Cement types	Detritus				Porosity	Stable isotope sample ID	δ^{18}O	δ^{13}C
										Amount & composition	Sa	Si	C				
	B	3	0.25	0.06	11.36	1.65 ± 0.04	80.63 ± 3.09	DC (p), Accept(2)							WD T0 iii	−3.4	−9.1
	B	7	0.28	0.08	8.48	1.63 ± 0.05	83.75 ± 4.34	DC (vp), Reject							ND	ND	ND
	B	8	0.24	0.03	18.79	1.68 ± 0.02	81.29 ± 1.90	DC (p), Accept(2)							ND	ND	ND
	D	9	0.39	0.53	2.12	1.51 ± 0.32	108.16 ± 29.79	DC (vp), Reject	mc, m-s (97% CaCO$_3$, 3% MgCO$_3$)	1% Q	•			1%	WD T0 iv	−5.9	−10.2
	D	10	0.36	0.48	2.00	1.61 ± 0.31	76.70 ± 26.63	DC (vp), Reject							WD T0 v	−5.0	−9.6
	D	11	0.38	0.28	3.61	1.50 ± 0.14	102.71 ± 13.42	DC (vp), Reject							WD T0 vi	−5.2	−11.1
	F	4	0.26	0.05	11.02	1.55 ± 0.03	74.81 ± 3.05	DC (p), Accept(2)	mc, m-s (97% CaCO$_3$, 3% MgCO$_3$)	1% Q, albite	•			1–10%	WD T0 vii	−7.1	−11.1
	F	5	0.23	0.04	15.09	1.55 ± 0.02	76.93 ± 2.23	DC (p), Accept(2)							WD T0 ix	−7.1	−12.1
	F	6	0.30	0.24	3.72	1.59 ± 0.15	112.23 ± 13.44	DC (vp), Reject							ND	ND	ND
	Average																
WD T10	C	1	0.45	0.02	38.21	1.35 ± 0.14	72.88 ± 0.85	DC, Accept (1)	mc, m-s (94% CaCO$_3$, 6% MgCO$_3$)	1% Q, microcline	•			<1%	WD T10 vii	−2.6	−8.3
	C	2	0.48	0.02	47.72	1.32 ± 0.25	68.38 ± 0.70	DC, Accept (1)							WD T10 viii	−2.1	−8.5
	C	3	0.48	0.02	58.13	1.34 ± 0.24	70.17 ± 0.61	DC, Accept (1)							WD T10 ix	−4.5	−10.3
	D	ND	ND	ND	ND	ND	ND	ND	mc, m-s (o-g), stain (p-e, m) (94% CaCO$_3$, 6% MgCO$_3$)	2–5% Q, anhydrite		•	•	3–7%	WD T10 iv	−7.3	−11.5
	D	ND	ND	ND	ND	ND	ND	ND							WD T10 v	−6.6	−10.8
	D	ND	ND	ND	ND	ND	ND	ND							WD T10 vi	−6.1	−10.4
WD T12	A	4	0.17	0.17	4.00	1.96 ± 0.24	205.53 ± 19.00	DC (vp), Reject	Not on thin section	Not on thin section	ND	ND	ND	ND	ND	ND	ND
	A	5	0.20	0.29	2.91	2.28 ± 0.48	295.32 ± 29.68	DC (vp), Reject							ND	ND	ND
	A	6	0.28	0.63	NC	NC	NC	DC (vp), Reject							ND	ND	ND
	D	ND	ND	ND	ND	ND	ND	ND	mc, m-s, stain (m) (94% CaCO$_3$, 6% MgCO$_3$)	1% Q,		•	•	1–5%	WD T12 ii	−9.3	−9.4
	D	ND	ND	ND	ND	ND	ND	ND							WD T12 iii	−9.6	−9.6
	G	1	0.22	0.26	3.07	1.79 ± 0.27	152.43 ± 19.50	DC (vp), Reject	mc, m-s (o-g), stain, fil (94% CaCO$_3$, 6% MgCO$_3$)	1% Q,		•		1–5%	ND	ND	ND
	G	2	0.18	0.12	5.61	1.80 ± 0.13	157.80 ± 9.38	DC (vp), Reject							ND	ND	ND
	G	3	0.16	0.09	5.79	1.74 ± 0.11	136.85 ± 19.50	DC (vp), Reject							ND	ND	ND
WD T13	A	ND	ND	ND	ND	ND	ND	ND	mc, m-s (og), stain (p-e, m) (97% CaCO$_3$, 3% MgCO$_3$)	1% Q, gypsum, muscovite, clinochlore, baddeleyite		•	•	1%	WD T13 iv	−3.1	−7.4
	A	ND	ND	ND	ND	ND	ND	ND							WD T13 v	−4.1	−8.5
	C	ND	ND	ND	ND	ND	ND	ND	mc, m-s, stain (p-e) (97% CaCO$_3$, 3% MgCO$_3$)	2–5% Q, microcline, muscovite, clinochlore, Palygorskite*		•	•	1%	WD T13 vii	−3.3	−7.8
	C	ND	ND	ND	ND	ND	ND	ND							WD T13 viii	−2.0	−6.6
	C	ND	ND	ND	ND	ND	ND	ND							WD T13 ix	−2.8	−7.6

Table 2 (*continued*)

Site	Band/layer	U–Th dating ID	^{238}U (ppm)	^{232}Th (ppm)	(^{230}Th/^{232}Th)	Initial (^{234}U/^{238}U)	Detrital corrected (bulk crust) age (ka) (2σ)	Comments	Cement types	Detritus Amount & composition	Sa	Si	C	Porosity	Stable isotope sample ID	δ^{18}O	δ^{13}C
	D	1	0.40	0.08	10.23	1.46 ± 0.03	69.38 ± 3.87	DC (vp), Reject (*)	mc, m-s (o-g) stain, fill	1% Q, clinachlore, palygorskite*			•	5–10%	WD T13 i	−3.2	−8.2
	D	2	0.36	0.08	10.11	1.46 ± 0.03	70.19 ± 3.96	DC (p), Reject (*)	(97% CaCO$_3$, 3% MgCaCO$_3$)						WD T13 ii	−1.9	−7.1
	D	3	0.38	0.09	9.55	1.47 ± 0.04	76.61 ± 4.46	DC (vp), Reject (*)							WD T13 iii	−1.9	−7.4
	D	4	0.30	0.08	9.08	1.51 ± 0.04	83.32 ± 4.98	DC (vp), Reject (*)							ND	ND	ND
WD T14	A	ND	ND	ND	ND	ND	ND	ND	mc, m-s (og) stain (m, p-e) (94% CaCO$_3$, 6% MgCaCO$_3$)	1% Q, baddeleyite, palygorskite		•	•	10–40%	WD T14 iv	−5.9	−7.3
	A		ND	ND	ND	ND	ND	ND							WD T14 v	−6.7	−8.0
	A		ND	ND	ND	ND	ND	ND							WD T14 vi	−5.6	−6.7
	D	2	0.19	0.04	14.07	1.59 ± 0.03	120.25 ± 3.20	DC (p), Accept(2)	mc, m-s (o-g), stain, fil	1–2% Q, baddeleyite, palygorskite*	•	•		10–40%	WD T14 i	−7.8	−9.6
	D	3	0.17	0.02	19.73	1.58 ± 0.02	109.96 ± 2.18	DC (p), Accept(2)	(94% CaCO$_3$, 6% MgCaCO$_3$)						WD T14 ii	−7.7	−9.3
	D	4	0.17	0.06	8.47	1.60 ± 0.06	133.80 ± 5.64	DC (vp), Reject (*)							WD T14 iii	−7.7	−9.4
	E	1	0.22	0.04	14.11	1.53 ± 0.03	93.79 ± 2.69	DC (p), Accept(2)	as layer D	1% (ND)		•		1–5%	ND	ND	ND
WD T8	B	ND	ND	ND	ND	ND	ND	ND	mc, stain (m) (94% CaCO$_3$, 6% MgCaCO$_3$)	1% Q			•	10–30%	WD T8 vii	−6.3	−6.8
	B		ND	ND	ND	ND	ND	ND							WD T8 viii	−6.1	−7.3
	B		ND	ND	ND	ND	ND	ND							WD T8 ix	−6.8	−6.8
	D		ND	ND	ND	ND	ND	ND	ND	mc, stain (m) (94% CaCO$_3$, 6% MgCaCO$_3$)	1% Q			•	3–5%	WD T8 iv	−6.8	−7.8
	D		ND	ND	ND	ND	ND	ND							WD T8 v	−6.4	−7.9
	D		ND	ND	ND	ND	ND	ND							WD T8 vi	−7.2	−7.3
	F	1	0.22	0.01	104.93	1.64 ± 0.01	98.26 ± 0.69	V clean	mc, m-s (o-g), fil (94% CaCO$_3$, 6% MgCaCO$_3$), 2.3% dolomite	1–2% Q, muscovite	•	•		1–3%	WD T8 ii	−5.6	−7.3
	F	2	0.27	0.01	102.13	1.64 ± 0.01	105.96 ± 0.80	V clean							WD T8 iii	−5.9	−7.1
	F	3	0.26	0.01	104.09	1.64 ± 0.01	107.57 ± 0.76	V clean							ND	ND	ND
WD T7	A	ND	ND	ND	ND	ND	ND	ND	mc, m-s (o-g), stain (m)	1–2% Q,	•	•	•	20–40%	WD T7 vii	−8.9	−12.7
	A		ND	ND	ND	ND	ND	ND							WD T7 viii	−8.6	−12.2
	B	7	0.23	0.01	49.07	1.67 ± 0.01	88.96 ± 1.32	DC (p), Accept(1)	mc, m-s (o-g), stain (m), fil (94% CaCO$_3$, 6% Mg CaCO$_3$)	1% Q,	•	•		1–3%	WD T7 i	−8.8	−12.9
	B	8	0.22	0.02	33.69	1.74 ± 0.02	85.50 ± 1.64	DC (p), Accept(1)							WD T7 ii	−10.1	−12.9
	B	9	0.22	0.02	34.16	1.71 ± 0.01	88.64 ± 1.52	DC (p), Accept(1)							WD T7 iii	−10.6	−12.8
	C	ND	ND	ND	ND	ND	ND	ND	mc, m-s (o-g) stain (m) (94% CaCO$_3$, 6% MgCaCO$_3$)	1% ND			•	10–30%	WD T7 iv	−8.8	−12.6
	C		ND	ND	ND	ND	ND	ND							WD T7 v	−8.7	−12.0
	C		ND	ND	ND	ND	ND	ND							WD T7 vi	−8.3	−11.6
	D	1	0.26	0.02	36.77	1.63 ± 0.01	81.95 ± 1.02	DC (p), Accept(1)	mc, m-s (incl o-g), occasional stain (m), fil (94% CaCO$_3$, 6% MgCaCO$_3$)	1% ND		•		1%	ND	ND	ND
	D	2	0.27	0.02	36.03	1.68 ± 0.01	91.15 ± 1.34	DC (p), Accept(1)							ND	ND	ND
	D	3	0.24	0.02	31.56	1.68 ± 0.01	85.81 ± 1.27	DC (p), Accept(1)							ND	ND	ND
	D	4	0.25	0.01	66.99	1.70 ± 0.01	85.75 ± 0.76	DC (p), Accept(1)							ND	ND	ND
	D	4R	0.22	0.02	24.54	1.68 ± 0.02	87.47 ± 1.72	DC (p), Accept(1)							ND	ND	ND

Table 2 (*continued*)

Site	Band/layer	U–Th dating ID	^{238}U (ppm)	^{232}Th (ppm)	$(^{230}Th/^{232}Th)$	Initial $(^{234}U/^{238}U)$	Detrital corrected (bulk crust) age (ka) (2σ)	Comments	Cement types	Detritus Amount & composition	Sa	Si	C	Porosity	Stable isotope sample ID	$\delta^{18}O$	$\delta^{13}C$
	D	5	0.23	0.02	28.31	1.68 ± 0.02	84.65 ± 1.48	DC (p), Accept(1)							ND	ND	ND
WD T11	D	1	0.24	0.02	28.33	1.66 ± 0.01	74.30 ± 1.15	DC (p), Accept(1)	mc, m-s (o-g), stain (m) & fil. (97% CaCO$_3$, 3% Mg CaCO$_3$)	2% Q, albite, baddeleyite	•	•		5–10%	ND	ND	ND
	D	2	0.25	0.02	25.33	1.68 ± 0.02	77.39 ± 1.35	DC (p), Accept(1)							ND	ND	ND
	D	3	0.24	0.02	36.05	1.70 ± 0.01	76.70 ± 1.08	DC (p), Accept(1)							ND	ND	ND
	I	ND	ND	ND	ND	ND	ND	ND	mc, m-s (o-g), stain (m) (97% CaCO$_3$, 3% Mg CaCO$_3$)	1% Q, muscovite		•	•	30–50%	WD T11 i	−3.2	−8.2
	I	ND	ND	ND	ND	ND	ND	ND							WD T11 ii	−1.9	−7.1
	I	ND	ND	ND	ND	ND	ND	ND							WD T11 iii	−1.9	−7.4
	J	ND	ND	ND	ND	ND	ND	ND	mc, m-s (o-g), stain (m) (97% CaCO$_3$, 3% Mg CaCO$_3$)	1% Q, albite			•	5%	WD T11 iv	−4.3	−9.9
	J	ND	ND	ND	ND	ND	ND	ND							WD T11 v	−3.3	−8.9
	J	ND	ND	ND	ND	ND	ND	ND							WD T11 vi	−2.6	−8.4
Surface of distal region rowhead																	
WD T3	ct	1	0.31	0.01	79.0	1.45 ± 0.01	98.74 ± 0.75	DC, Accept (1)	mc, m-s (p-e & some o-g), & fi. (97% CaCO$_3$, 3% Mg CaCO$_3$)	<1% Q			•	5–10%	WD T3 i	−4.7	−9.1
	ct	2	0.31	0.02	31.9	1.45 ± 0.01	98.78 ± 1.31	DC (p), Accept(1)							WDT 3 ii	−3.3	−6.9
	ct	3	0.30	0.01	82.2	1.51 ± 0.01	111.73 ± 0.83	DC, Accept (1)									
	Average						**103.2 ± 1.6**										

ND means data not determined for that band//layer.

In "Comments" column: DC = detrital correction and addition of (p) is poor, and (vp) is very poor. "Accept(1)" where $(^{230}Th/^{232}Th)$ is > 20 and bulk crust detrital correction seems sensible, "Accept(2)" means accept with a lower cut-off for $(^{230}Th/^{232}Th)$ ~10 < 20) (*) relates to presence of palygorskite (see detritus column).

In "Cement Types" column: mc = micrite, m-s = microspar, (o-g) = overgrowth; stain, with (pe) for pore edges and (m) for within the matrix; fil = microbial filaments are observed.

For "Detritus": Q = quartz and the columns Sa = sand, Si = silt and C = clay for the sizes of particles observed in thin section, with [•] to indicate presence. *palygorskite indicates possible biomineralisation in the tufa fabric, which could relate to fabric alteration, and this is another ground for rejection.

samples (see Supp. Info. 3 for illustrations), and acted as an additional check on our acceptance criteria. For example, whilst two sub-samples of band/layer D in WD T13, fell in the (^{230}Th/^{232}Th) lower cut off, the high level of microspar overgrowth in the cement, the staining and the presence of palygorskite suggested these samples likely diverged furthest from closed-system behaviour. While the accuracy of data from some individual subsamples may be called into question, there is broad agreement in U–Th dates obtained from multiple sub-samples within the same band/layer within our analysed tufa. This suggests that, taken as a whole, the dataset presented here is of sufficient quality to assign tufa growth to individual marine isotope stages.

Using averages for accepted subsamples, tufa deposition occurred: (i) in MIS 7 (WD T4, 211.1 ± 7.6 ka), (ii) at the transition from MIS 6 to 5e (WD T5, 135.7 ± 6.9 ka and WD T6, 128.4 ± 3.1 ka), and (iii) within MIS 5 (WD T14 band/layer D, 115.1 ± 3.8 ka; WD T3 of 103.2 ± 1.6 ka, WD T14 band/layer D, 93.8 ± 2.7 ka; WD T7 band/layer B, 87.7 ± 2.2 ka; WDT7 band/layer D, 86.1 ± 1.7 ka, WDT0 band/layer B, 81.0 ± 3.6 ka; WDT0 band/layer F, 75.9 ± 3.6 ka; WD T11, 76.1 ± 1.8 ka, WD T13, 73.8 ± 4.5 ka and WD T10, 70.5 ± 1.1 ka). Deposition within MIS 5 does not cluster at interglacial sub-stages (dashed lines, Fig. 2), but can be grouped into early (WD T14), middle (WD T3, WD T14 band/layer E) and late (WD T7, with WD T11, T13 and T10 close to the transition from MIS 5 to 4). In addition, ages are stratigraphically sensible at the landscape-system scale, with the vug-fill tufa (WD T4) within the fossil tufa cascade at the lowest elevation site recording MIS 7 ages, then MIS 6/5.5 ages within the north bank of the southern wadi channel exposure, which is ~1.5 m below the basin surface, and MIS 5 ages for tufa preserved at the surface of the main basin and the surface of the distal-region (see Fig. 1C, Table 1 and Supp. Info. 2). Linking back to Table 1, this makes unit 2iii in the fossil tufa cascade (WD T4) the oldest dated unit, deposited in MIS 7, meaning that underlying units 2ii and 2i could be older still. The next oldest is unit 3iii in the southern wadi channel exposure (WD T5 and T6), deposited at the transition from MIS 6 to 5e (WD T5 and T6), and units 3i and 3ii are likely older still. Units 2iv and unit 3i hypothesised to be of the same depositional age, could be so, particularly if unit 2iv and units 3i and 3ii were also part of the MIS 7 phase of tufa deposition.

δ^{18}O ranges from −14.6 to −1.9‰. When considered alongside δ^{13}C (Fig. 3A), there are three broad groups in δ^{18}O: (1) those with the lowest δ^{13}C values compared to δ^{18}O values, co-varying with a linear-regression line slope of 0.92 (WD T0, 10, 12, 13, WD T7 and 11 on basin surface and WD T3 surface coating), (2) a second co-varying group with a linear-regression line slope of 0.88, but higher δ^{13}C values (WD T14, T8 on the basin surface and WD T3 main sample and WD T4 on the fan) and (3) a group with no isotopic covariance (WD T5 and T6 in the incised channel) (Fig. 3A). Co-variation in the two isotopes can be indicative of an evaporative enrichment effect on the two isotopes, which implies a non-evaporated source would have had even more negative values. The three groups have some associated age clustering; group 3 is the MIS 6/5e transition, group 2 has MIS 7 and middle MIS 5, and group 1 are late MIS 5 and MIS 5/4 (Fig. 3B). Furthermore, the temporal groupings have a striking similarity to the trends in isotopic depletion/enrichment observed in the speleothems in Mukalla Cave, Yemen and Hoti Cave, Oman (Fleitmann et al., 2011) (Fig. 3C). That is to say that in both the Wadi Dabsa tufa sequence and the southern Arabian speleothem records, the carbonates dating to MIS 5e, and the MIS 6/5e transition, record the lowest δ^{18}O values, whilst those carbonates dated to the later sub-stages of MIS 5 contain the highest δ^{18}O values. In all three regions the δ^{18}O values from samples dated to MIS 7 lie between those of MIS 5e and those of middle/late MIS 5.

δ^{13}C ranges for −12.9 to −6.3‰, which is in the range for cool-water tufa (Fig. 3), in contrast to +2 to +8‰ observed in thermogene travertines (e.g. Capezzouli et al., 2014). A non-thermal origin is supported by the interpretation of tufa ^{87}Sr/^{86}Sr isotopic ratios in these samples by Stone et al. (2022). δ^{13}C are isotopically lighter than the signatures observed in tufa from the western desert of Egypt (Fig. 3A) (Crombie

et al., 1997; Smith et al., 2004; Kieniewicz and Smith, 2009; Brookes, 2010; Jimenez, 2014; Kele et al., 2021). There is some overlap of δ^{13}C with Wadi sites in the eastern desert (Wadi Gemal and Wadi Abu Had) (Hamdan and Brook, 2015) as well as Wadi Watier (Hamdan and Brook, 2015) and Bet Shean (Kronfeld et al., 1988) in the Sinai and Levant (Fig. 3A).

5. Discussion

5.1. Timing of tufa deposition within the regional context

The dominance of interglacial deposition (in MIS 7 and MIS 5) of Wadi Dabsa tufa (Fig. 2, Fig. 4J) is consistent with the temporal trend recorded in speleothem deposition in Mukalla Cave, Yemen and Hoti Cave, Oman (Burns et al., 2001; Fleitmann et al., 2003a, 2003b, 2007, 2011), from which Southern Arabian Humid Periods (SAHP) (green bars Fig. 4H) are defined (Nicholson et al., 2020). SAHP 6 to 1 are broadly coeval with MIS 7e, MIS 7a-c, MIS 5e, MIS5c, MIS5a and MIS1 (the Holocene) respectively. Many of the sapropel layers in the Mediterranean Sea align with the timing of SAHPs (S1, S3, S4, S5, S7 and S9 aligning with SAHPs 1, 3, 5 and 6 respectively) (Fig. 4D,H), associated with freshwater discharge into the (eastern) Mediterranean Sea during increased ASM strength and with less clear contributions from elsewhere on-land in the Mediterranean or from enhanced Mediterranean moisture flux (Rohling et al., 2015). There is overlap between tufa deposition at Wadi Dabsa and SAHP 5, 4, 3 and 2 (Fig. 4). The temporal resolution achievable for U–Th dating of these speleothems means that sub-stage patterns within MIS 7 and MIS 5 are not resolved (Fig. 2). The model for a lack of precession-driven speleothem growth (or SAHPs) during glacial periods in Hoti and Mukalla speleothems was interpreted as indicating an impediment of the northward movement of ISM rains (and the ITCZ) onto the Arabian Peninsula during glacial periods (Fleitmann et al., 2011).

Tufa in the incised wadi channel (WD T6 and T5) include late MIS 6 ages (Figs. 2 and 4J), although noting that within age uncertainties these overlap with early MIS 5 at 1 standard deviation. In their review of pluvial periods in southern Arabia, Nicholson et al. (2020) acknowledge some MIS 6 ages for fluvio-lacustrine sediment deposition in Arabia including late MIS 6, (Fig. 4I). This is also observed in the timing of Negev speleothem deposition (Fig. 4H), as well as the timing of tufa deposition in north Africa (Fig. 4J). Arranging these humidity records by latitude and longitude for each proxy type (speleothem, lacustrine and fluvial, tufa), reveals some tentative spatial patterns. For example, for lacustrine-and-fluvial records this is recorded north of 28.0°N (and west of 41.3°E), whilst in the south there are a few ages close to the MIS 6/5 transition (Fig. 4I). It is not yet clear whether this is a definitive spatial pattern or an artifact of the depths to which samples have been retrieved within current field sampling strategies in the Rub' al Khali. The northern sites that include MIS 6 ages include: (i) the Mudawwara depression, southern Jordan, with U–Th ages of Cardium shell-bed sediments of 170 + 14/-13 ka, 152 + 8/-7 ka and 135 ± 6 ka (Petit-Maire et al., 2010) (Fig. 4I, latitude 29.5°N, longitude 36.0°E), (ii) the southwest lake at Khall Amayshan 4 (KAM4) Basin, with a fine-grain quartz luminescence age for a lacustrine unit in the southwest lake of 143 ± 10 ka, dating to "either late MIS 6, or less probably, to the transition to MIS 5" (Groucutt et al., 2021, p377) with underlying sands of 184 ± 14 ka (Fig. 4I, latitude 28.0°N, longitude 39.5°E), (iii) the south lake and south east lake at KAM4 with course-grain quartz luminescence ages for basal sands of 168 ± 12 ka and 142 ± 13 ka and of 154 ± 11 ka and 149 ± 9 ka respectively (Groucutt et al., 2021) (Fig. 4I, latitude 28.0°N, longitude 39.5°E), and (iv) aeolian sands beneath lake deposits at site 11.5 (40 km east of Jubbah) dated using coarse-grained quartz luminescence dating to 177 ± 13 ka (Rosenberg et al., 2013) (Fig. 4I, latitude 28.0°N, longitude 41.4°E). Within the Jubbah Basin itself, there is a (non-fading corrected) feldspar pIRIR$_{290}$ luminescence age of 135.8 ± 23.9 ka (corrected 166.1 ± 38.9 ka) (Clark-Balzan et al., 2018), which
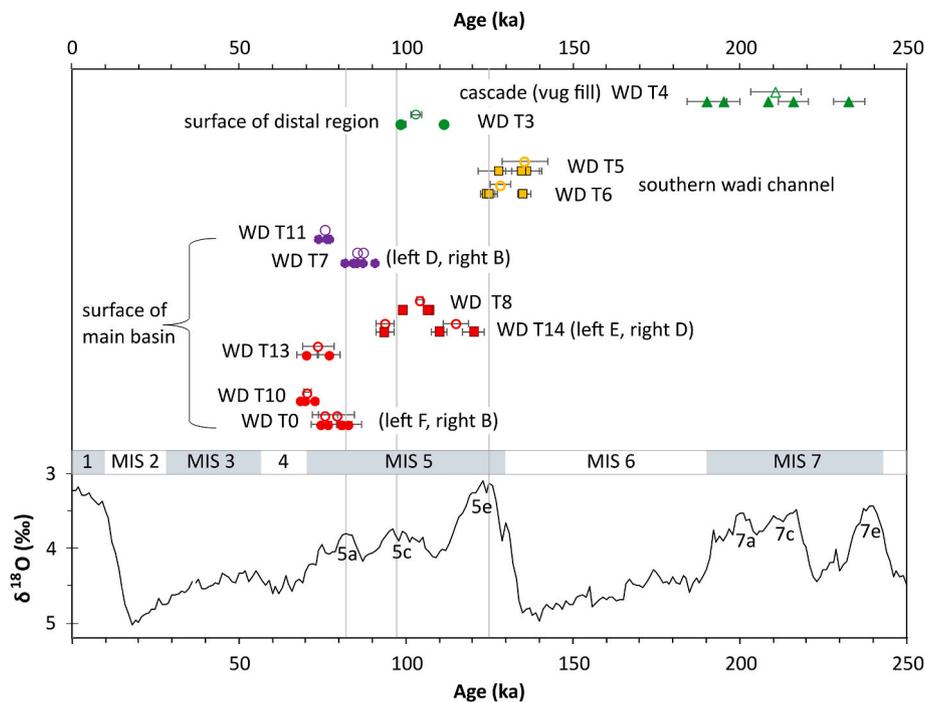
Fig. 2. U–Th ages for the Dabsa tufa by location, where solid symbols are accepted sub-sample ages, and open-symbols are averages for those samples (see Supp. Info 3 for detailed of U–Th subsampling locations on each sample).

overlaps with MIS 5 and the younger age is preferred by Clark-Balzan et al. (2018) and Parton et al. (2018) (Fig. 4I, latitude 28.0°N, longitude 41.1°E). In the south of interior, the Khujaymah palaeolake (western Rub' al Khali) has TT-OSL luminescence ages of 136 ± 14 ka, 138 ± 11 ka, 143 ± 11 ka, 144 ± 9 ka and 147 ± 15 ka (Rosenberg et al., 2011) at the MIS 6/5 transition (Fig. 4I, latitude 18.6°N, longitude 47.2°E).

In the speleothem record, there are early MIS 6 U–Th ages (perhaps overlapping with late MIS 7) in the north of the study region (Fig. 4H) within the Negev (194.8 ± 3.4 ka at Ashalim Cave, 187.5 ± 2.4 ka at Hol-Zakh Cave) and later in MIS 6 (157.2 ± 3.8 ka at Maktesh-ha-Qatan Cave and 140.1 ± 3.5 and 138 ± 4.1 ka at Ma'ale-ha-Qatan Cave) (Vaks et al., 2010) (Fig. 4H, latitude 31.0°N, longitude 35.0°E). In contrast, the Hoti and Mukalla Cave records are more tightly constrained to MIS 7 and MIS 5, with one U–Th age for Hoti Cave at the MIS 6/5 transition (134 ± 4.2 ka) (Fig. 4H) (Burns et al., 2001). Within the tufa record (Fig. 4J) there are U–Th ages across MIS 6 in north Africa, as far as 29.6°E in Egypt (Kurkur Oasis (Kele et al., 2021), Kharga Oasis (Sultan et al., 1997; Smith et al., 2004, 2007; Kleindienst et al., 2008; Kleindienst et al., 2009; Abotalib et al., 2019) and Daklah Oasis (Kleindienst et al., 2009)) (Fig. 4J latitudinal range 23.5–25.0°N, longitudinal range 28.6–32.3°E). Within the tufa dataset the late MIS 6 U–Th ages include: 159 ± 1 ka, 146 ± 1 ka and 144 ± 1 ka (at Kharga and Kurkur Oasis) (Abotalib et al., 2019); 166 ± 2 ka Refus Pass, Kharga Oasis (Kleindienst et al., 2008; Kleindienst et al., 2009), 145 ± 6 ka Dakleh Oasis (Kleindienst et al., 2009), 150 ± 13 ka, 142 ± 0.3 ka and 140 ± 1.2 ka at Kharga Oasis (Smith et al., 2004) and also 157 ± 12 ka at Kharga Oasis (Sultan et al., 1997). The wet-dry index within the eastern Mediterranean core OD967 (derived from principal components analysis of XRF data) suggests the majority of MIS 6 was more humid than today (Fig. 4E), whereas the probability density curves for Saharan and Arabian humidity (based on dated lacustrine, fluvial, palaeosol, calcrete, speleothem, tufa/travertine and sinter sediments) suggest the humidity of MIS 6 was similar to MIS 7 but lower than that of MIS 5 (Drake et al., 2013) (Fig. 4F).

The timing of MIS 6 humidity across this wider region requires some consideration. Parton et al. (2015) and Nicholson et al. (2020) suggest that surface hydrological systems may respond to a lower precipitation

threshold (~200 mm/y) than that required for aquifer recharge and subsequent speleothem growth (>300 mm/y) at Hoti and Mukallah Caves (Fleitmann et al., 2011). The fact that the Wadi Dabsa tufa units within the incised wadi channel (WD T6 and T5) overlap with the transition between MIS 6/5e could represent activation of a shallow-groundwater to surface water tufa system under a similarly lower precipitation threshold, assuming that ages are not to be considered to fall within MIS 5 within error estimates. Within northern Africa, Abotalib et al. (2016), Abotalib et al. (2019) consider the timing of western desert tufa in Egypt and explore the idea of time-lags in the north-to-south groundwater flow paths, with a lag of ~10 ka at the end of a wet period, which could account for some of the early MIS 6 'glacial period' tufas. In contrast, Kele et al. (2021) account for tufa deposition during glacial periods via a change in atmospheric circulation patterns, driven by the influence that lower sea levels had on the formation of an Indian Ocean Warm Pool, which forced higher precipitation. Fundamentally, our ability to precisely correlate the timing of the formation of surficial deposits to specific climate stages is limited by the associated uncertainties of the chronological techniques applied and exacerbated when these sediment sequences form close to a climatic transition.

It remains difficult to conclusively unpick the role of different rainfall regimes during MIS 6 and MIS 5 across the Saharo-Arabian region based on the timing of humidity proxies alone. Individual atmospheric circulation systems will generate rainfall with different $\delta^{18}O$ values, potentially allowing $\delta^{18}O$ to be used as a tracer for climate systems. However, in the surficial environment the $\delta^{18}O$ freshwater carbonates is a function of both 1) the $\delta^{18}O$ of meteoric water, and 2) the temperature at which carbonates mineralise. As the latter value is never known (for surficial carbonates in dryland regions at least) it is difficult to come to a reliable conclusion about the $\delta^{18}O$ of the source water from the $\delta^{18}O$ of the carbonates. It is hoped that such questions may be resolved in the future using methodological developments in stable isotopic methods, such as clumped isotopic measurements for tufa (e.g. Kele et al., 2021) and speleothem fluid inclusion analysis (e.g. Fleitmann et al., 2003b; Rogerson et al., 2019; Nicholson et al., 2020), which allow the direct measurement or calculation of the $\delta^{18}O$ of water.

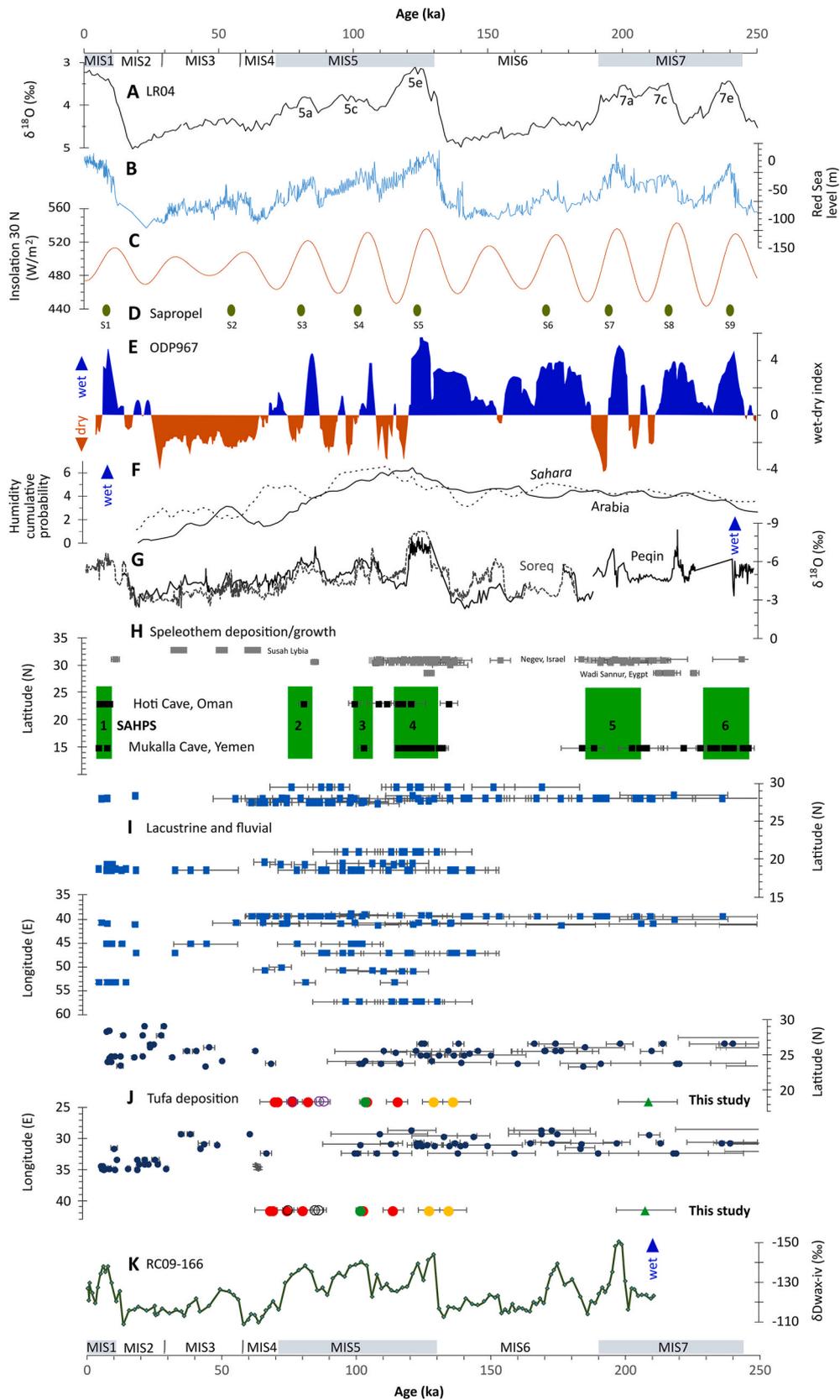Further proxy evidence for last interglacial conditions close to Wadi
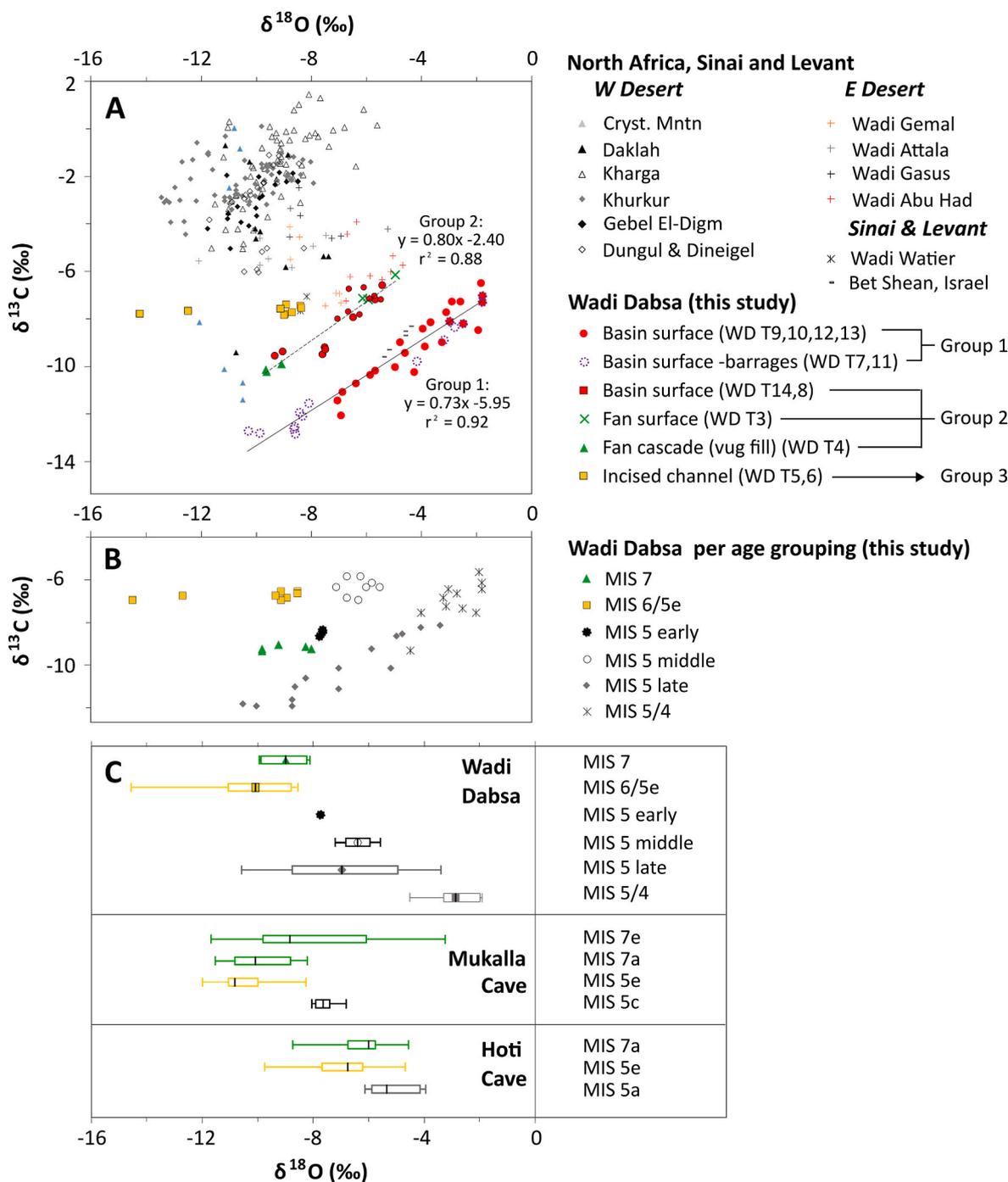
Fig. 3. Stable isotopic composition (A) at Wadi Dabsa tufa in comparison to other tufa in north African and the Levant for oxygen and carbon, (B) at Wadi Dabsa, grouped by sample age and (C) for oxygen only, using boxplots for the age groups at Wadi Dabsa alongside the data from speleothems in Mukalla Cave in Yemen and Hoti Cave in Oman (Fleitmann et al., 2011).

Dabsa are provided at Dhahaban quarry (25~ km SSE of Wadi Dabsa) (Fig. 1B). Here there are luminescence ages for a sequence of indurated marine sands, covered by shell sand and aeolianite/beachrock (Sanderson and Kinnaird, 2019). Marine sands indicate higher sea-level than present at this site (~1–2 km from the current coast). Whilst ages are close to quartz luminescence saturation, with a high overdispersion of single aliquot age estimates, some samples contain aliquots consistent with an MIS 5e age, with no subsequent uplift (Sanderson and Kinnaird, 2019). There are also aliquots consistent with MIS 5c requiring 0.2 mm/y uplift and MIS 5a requiring 0.5 mm/y uplift.

There is less terrestrial evidence for wetter MIS 7 conditions than

earlier phases, beyond that in the Mukalla and Hoti speleothems. There are ages within some lacustrine sites in the Nefud Desert at Jubbah (Rosenberg et al., 2013; Clark-Balzan et al., 2018; Parton et al., 2018) and the Northwest Lake at KAM4 (Groucutt et al., 2021), and all but one of these (from Rosenberg et al., 2013) fall in MIS 7a (Fig. 4I). The two dated horizons at the Acheulean site of Saffaqah, Dawadmi region, central Saudi Arabia also fall within MIS 7, and although the palaeoenvironmental nature of those deposits has not been constrained, this landscape contains small relict fluvial channels and the site is located between the Wadi al Batin and Wadi Sabha catchments (Scerri et al., 2018; Shipton et al., 2018).

(caption on next page)

Beyond the Saharo-Arabian belt there is a striking similarity with the timing of tufa deposition in Europe. For example, ages for tufa in the southern Dinarides Karst region of Croatia (Plitvice Lakes and the Krka River) are clustered in interglacials MIS 9, MIS 7 and MIS 5, with only a handful of ages falling within MIS 8 and MIS 6 glacials (Horvatiničič et al., 2000). Further west in central Spain (Tagus River and tributaries) eight main tufa-deposition ages were distinguished on the basis of U–Th dating by Oritz et al. (2009), during MIS 11, MIS 7e and 7a, MIS 6-5e, MIS 3 and the Holocene. A similar temporal pattern is seen for the Añamaza, Mesa, Piedra and Ebrón river valleys in northeast Spain, where tufa deposition occurs during MIS 11, MIS 7 and the warmest substages of MIS 5 (5.5, 5.4 and 5.1), but also during MIS 6 (Sancho et al., 2015). In northern France, tufa of the Somme River is U–Th dated to MIS 5 (Antoine et al., 2003, 2006). There is evidence for a widespread humid interval across the Mediterranean during MIS 6.5, as recorded in lacustrine carbonate δ^{18}O from the Ioannina basin of NW Greece (Wilson et al., 2013). This points toward a northern-hemisphere-wide increase in moisture during interglacial periods.

5.2. Oxygen isotopic signatures of Wadi Dabsa tufa within the regional context

The δ^{18}O value of tufa carbonate is controlled by three main factors: 1) the δ^{18}O value of the precipitation that occurred during the interval of tufa formation, 2) any modification of the δ^{18}O signal as the water moves through the surface and sub-surface system, and 3) the temperature at which carbonate mineralisation occurred (Andrews, 2006; Capezzouli et al., 2014). In latitudes such as the Arabian Peninsula, the main controls on δ^{18}O in precipitation are the amount of precipitation (with wetter climates resulting in rainfall with lower δ^{18}O values) and the source of the atmospheric moisture (Rozanski et al., 1992, 1993; Fleitmann et al., 2011; Nicholson et al., 2020). In the sub-surface/surface environment (Groucutt et al., 2018), the δ^{18}O value of meteoric water can be changed by varying degrees of mixing of rainfall, from different seasons for example, and evaporation in the surface environment. The temperature control on isotopic fractionation during carbonate formation is well-understood and occurs at around 0.3 ‰/+1 °C (Hays and Grossman, 1991; Kim and O'Neil, 1997).

In the isotopic analysis of carbonates formed in low latitude semi-arid/arid regions, shifts in δ^{18}O values have been interpreted within the context of shifts in humidity/aridity, with carbonates that have formed under more humid conditions being characterised by lower δ^{18}O values (e.g. Nicholson et al., 2020). This is partly because of the amount effect (Rozanski et al., 1992, 1993), described above, but also partly because of the tendency, under humid climates, for there to be lower rates of evaporation in surface waters (Candy et al., 2012). As evaporation leads to an increase in δ^{18}O values within surface waters, more arid climates lead to more positive δ^{18}O values in carbonates, whilst the reverse is true for carbonates forming under more humid conditions (Candy et al., 2012). Within this framework the simplest interpretation of the Wadi Dabsa U–Th dated δ^{18}O dataset would be that humid phases, as recorded by the timing of tufa formation, occurred during MIS 7, the MIS 6/5e transition and during the middle and late stages of MIS 5, and

MIS 2. Furthermore, of these: (i) the most humid was that which spanned MIS 6/5e, (ii) the driest occurred in the middle/late parts of MIS 5, whilst (iii) the humid phase in MIS 7 would have been of intermediate humidity between these two end members. This is consistent with the patterns/trends seen in speleothem records from southern Arabia δ^{18}O, where patterns across these humid periods are interpreted as reflecting changing moisture regimes (e.g. Fleitmann et al., 2011; Nicholson et al., 2020). It is also significant that, in general terms, the absolute values of the δ^{18}O signature in Wadi Dabsa tufa are consistent with those from southern Arabian speleothem records in MIS 7, MIS 6/5e and middle/later MIS 5 (Nicholson et al., 2020).

The U–Th ages and δ^{18}O signatures presented here, therefore, suggest that the region of Wadi Dabsa (southwestern Arabia, Red Sea coast) experienced a history of humid phases that was similar to that of Mukulla and Hoti Caves (southern Arabia). Whilst the consistency in the timing of major humid phases across the region is not surprising, the δ^{18}O evidence would suggest that not only did the same distribution of humidity exist within the humid phases preserved in these regions but also that these regions were, during each humid phase, influenced by the same air masses. The latter point is suggested simply because if the regions were affected by different air masses then the different source areas of each systems would likely produce rainfall with very different δ^{18}O values. Across the wider Saharo-Arabian belt, there is of course, a more-complicated geographic pattern involving a range of rainfall sources and regimes during the same time-periods, as well as the potential for different climatic-forcing of rainfall regimes during glacial-periods as compared to interglacials. For example, as recently highlighted by Kele et al. (2021) in the context of tufa in northern Africa.

For the first time it is possible to propose a consistent palaeoclimatic history between the southern and western coasts of the Arabian Peninsula. This is in agreement with climate simulations for MIS 5e that show both a strong increase in both mean annual (Fig. 5B) precipitation, and summer (JJA) precipitation (Fig. 5C) (Otto-Bliesner et al., 2006; World Clim, 2015) (Fig. 5A), and modelled δ^{18}O of −7 to −6‰ at the location of Wadi Dabsa (Herold and Lohmann, 2009; Gierz et al., 2017) (Fig. 5A). The most depleted δ^{18}O in the model is spatially concentrated in the northwest of the horn of Africa, with a zone < −7‰ extending west into central north Africa (Fig. 5A). There are zones of simulated precipitation of > 400 mm/y on the Arabian Peninsula, including Yemen and the western coast of Saudi Arabia from the latitude of Wadi Dabsa up to ~26°N, where this stretches inland, with > 300 mm/y covering many of the Nefud desert sites in Fig. 1. The JJA spatial pattern is broadly similar. The location of Wadi Dabsa is modelled to have ~480 mm/y (and 240 mm of rainfall during JJA), with 433 mm/y (245 mm during JJA) at Mukalla Cave, and 212 mm/y (159 mm in JJA) at Hoti Cave.

It is worth noting that a direct comparison between the δ^{18}O value of two carbonate types that form in different hydrological contexts (i.e. cave versus surface water environments) can be problematic. Intra-system processes that may lead to isotopic modification may not be comparable. It is likely, for example, that the greater spread in δ^{18}O values which occurs in the Wadi Dabsa tufa dataset is a function of the impact of evaporation on surface waters, a process that is likely to be less significant in cave settings. However, despite this, it is argued that
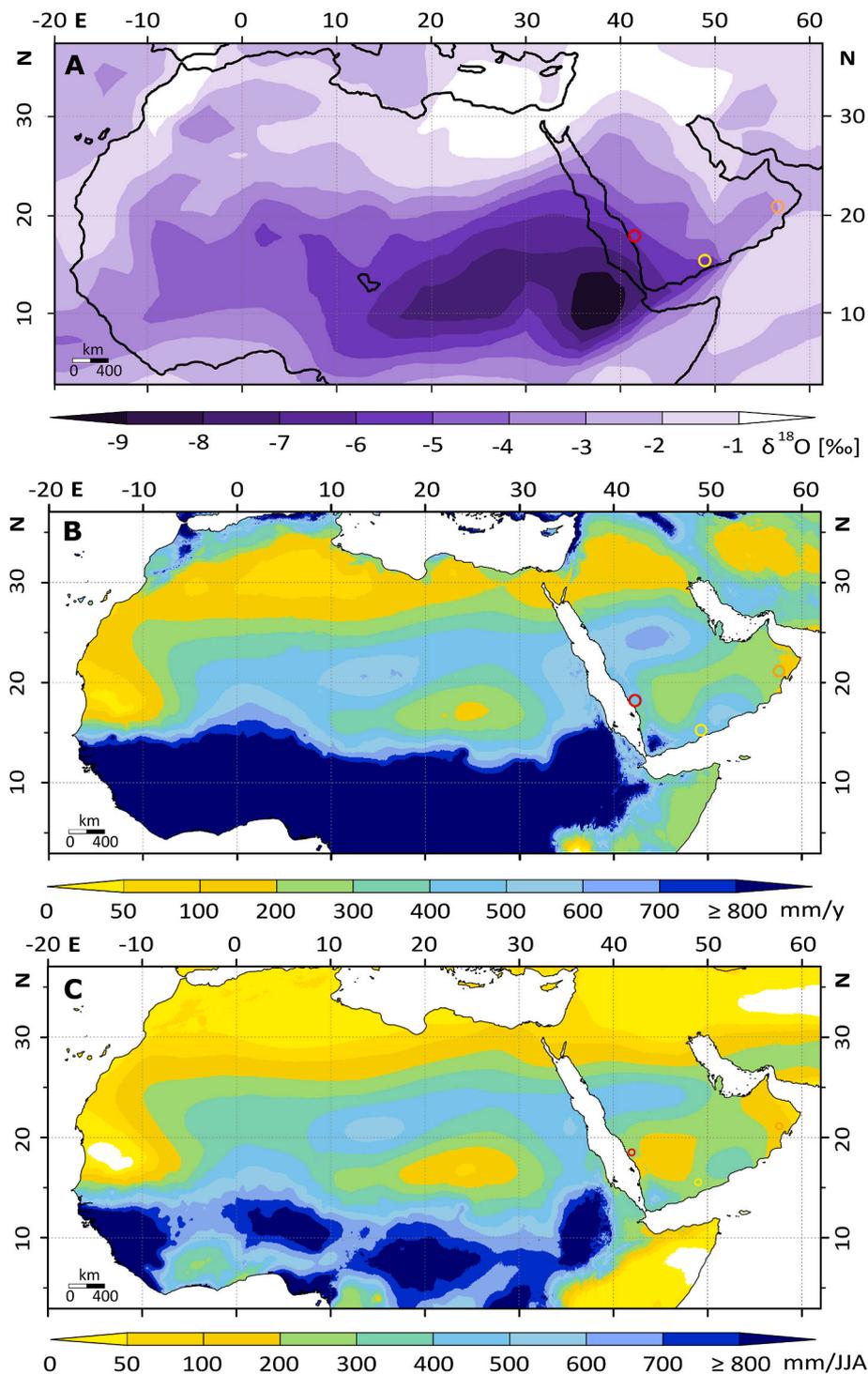
Fig. 5. Simulations outputs for MIS 5e of (A) δ^{18}O for boreal summer precipitation (modified after Herold and Lohmann, 2009). Each map shows the locations of Wadi Dabsa Wadi Dabsa (red circle) and Mukalla Cave (yellow circle) and Hoti Cave (orange circle), (B)mean annual precipitation and (C) boreal summer (JJA) precipitation for the Saharo-Arabian belt (plotted in R using data from Otto-Bliesner et al., 2006; World-Clim, 2015).

comparison of tufa and speleothem isotopic datasets in this study is meaningful for climate reconstruction. This case is made because there is limited evidence for systematic variation in δ^{18}O values within these analysed tufa facies, negating the possibility/likelihood that tufa depositional processes, rather than prevailing climate, are controlling the isotopic signal. Equally, even where there is isotopic evidence for evaporitic modification of δ^{18}O values in the Wadi Dabsa sequence this is only found in the humid phases proposed to be less humid, therefore supporting this interpretation.

There are wider datasets of δ^{18}O in speleothem and tufa available across the Saharo-Arabian belt (Fig. 2A and 6). However, the vast majority of these data do not have corresponding age control, which limits our ability to further interrogate the temporal trends in humidity extremes, as well as any attempt to explore spatial patterning that might cast light on the role of different rainfall regimes across space and through time. We follow Kele et al.'s (2021) approach to compare the ranges in δ^{18}O (for all/any age of carbonate) alongside our new data from Wadi Dabsa in Fig. 6 but plot the data by both latitude and
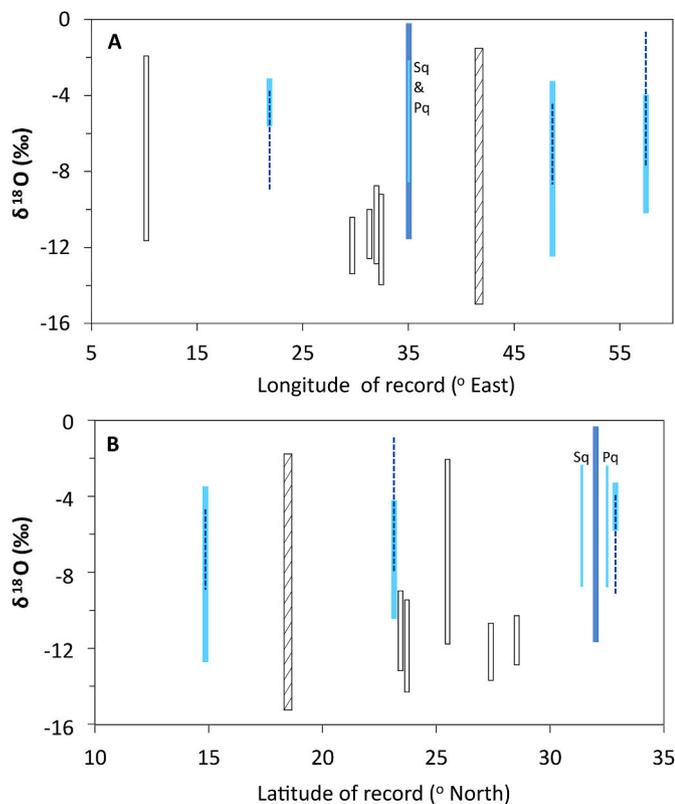
Fig. 6. Stable oxygen values for tufa and speleothem carbonates for Wadi Dabsa tufa this study (bar with horizontal hatching), and a range of other sites, arranged by (A) longitude and (B) latitude (blue bars are speleothem carbonate, and dashed dark blue lines are fluid inclusion data for the speleothems where this is available, the grouped Negev Caves record is in a darker blue, to be distinguished from Soreq Cave (Sq) and Peqin Cave (Pq) at the same longitude on plot (A), white boxes with black outlines are tufa carbonate samples. From south to north, plot (B), these are Mukalla Cave (Fleitmann et al., 2011; Nicholson et al., 2020); Wadi Dabsa (this study); Hoti Cave (Fleitmann et al., 2011; Nicholson et al., 2020); Dungul and Dineigl Oases (Kele et al., 2021); Kurkur Oases (Crombie et al., 1997); Tadrart Acacus (Cremaschi et al., 2010); Djara Cave (Brook et al., 2002); Wadi Sunnur Cave (El-Shenawy et al., 2018); Soreq Cave (Ayalon et al., 2002; Bar-Matthews et al., 1997, 2003; Bar-Matthews and Ayalon, 2004); Negev desert caves from a range of locations (Vaks et al., 2006, 2010, 2013); Peqin Cave (Ayalon et al., 2002; Bar-Matthews et al., 1997, 2003; Bar-Matthews and Ayalon, 2004) and Susah Cave (Rogerson et al., 2019).

longitude. Kele et al. (2021) had identified two groups of sites. The first has data with $\delta^{18}O < -9\permil$ (Djara Cave, Egypt (site 42, Fig. 1); Wadi Sannur Cave, Egypt (site 43, Fig. 1); the Kurkur-Dineigl-Dungul Oases, Egypt (sites 36,37, Fig. 1). This contrasts with sites having, or having a range that extends to, more positive values (Susah Cave, Libya (site 44, Fig. 1); Tadrart Acacus tufa, Libya (site 45, further west than field of view in Fig. 1); Peqin and Soreq Caves (sites 25 and 26, Fig. 1); speleothems in the Negev (sites labelled 27 in Fig. 1). From this they suggest there are at least two hydrological provinces affecting their southern Egyptian tufa sites. The first is isotopically depleted (they term this 'Mashriqian') and the second is isotopically enriched (they term this 'Maghrebian'). The enriched group is considered to be 'probably westerly' and involving both Atlantic and Mediterranean source moisture, whilst the depleted group may reflect ISM but also have an influence of Indian Ocean Warm Pool-forced precipitation, for which forcing is expected to be strongest during glacial low sea level stands (Kele et al., 2021). The distribution of the $\delta^{18}O$ data by longitude (Fig. 6A) does not confirm these suggestions, with no clear west-east pattern of lower and upper ranges for $\delta^{18}O$. Similarly, when plotted by latitude (Fig. 6B) there are no striking south-north trends to $\delta^{18}O$ minima and maxima. The lack

of chronological control for different samples within these $\delta^{18}O$ ranges (Fig. 6) means that it is not possible to assess whether enrichment/depletion trends are synchronous or asynchronous across the landscape, and overall it remains difficult to fully understand what this means for atmospheric circulation patterns. The best way forward in unpicking moisture source regions coms from combining $\delta^{18}O$ and δD from fluid inclusions speleothems accompanied by their well-constrained chronologies and comparing them to modern meteoric waterlines (e.g. Fleitmann et al., 2003b; Rogerson et al., 2019; Nicholson et al., 2020).

5.3. Carbon isotopic signatures of Wadi Dabsa tufa within the regional context

Most studies that utilise the $\delta^{18}O$ and $\delta^{13}C$ values of freshwater and terrestrial carbonates as a basis for palaeoenvironmental interpretation focus on the systematics of oxygen isotopes. This is because the $\delta^{18}O$ value of a carbonate is strongly controlled by the $\delta^{18}O$ composition of the meteoric water that it mineralises from which is, in turn, controlled by a range of environmental factors such as bedrock geology, temperature, precipitation amount and evaporation. In contrast the $\delta^{13}C$ value of such carbonates is controlled by more local factors such as soil processes, vegetation type and cover, groundwater residence time and rates of degassing (Andrews et al., 1997; Andrews, 2006). Stone et al. (2022) have highlighted that the geochemistry of the Wadi Dabsa tufas are indicative of meteogene carbonates fed by shallow groundwater aquifers. The range of $\delta^{13}C$ values are typical of those recorded in modern and Pleistocene tufas that formed in perennial water bodies under temperate climates and well-vegetated catchments (Andrews et al., 1997; Andrews, 2006; Dabkowski et al., 2012, 2013). Dankowski et al. (2012; 2013) interpret variability of a function of $\delta^{13}C$ in interglacial age tufa to be due to: 1) the evolution of climate, vegetation and aquifer conditions during the warm period and 2) differences in the geochemical processes associated with different tufa facies. With reference to the first point, the development and maturation of soil profiles during an interglacial will lead to an increase in the amount of soil respired CO_2 provided to the carbon pool. With reference to the second point, shallower and wider water flows will result in greater amounts of degassing than that which would typically occur in deeper water conditions. It is likely that a combination of such factors can explain the range of $\delta^{13}C$ values seen at Wadi Dabsa.

The difference between the $\delta^{13}C$ values of the Wadi Dabsa tufa and those of previously studied tufa from the western desert of Egypt is informative. The $\delta^{13}C$ values of the former (-6.3 to $-12.9\permil$ VPDB) are consistently more negative than those of the latter (-6.0 to $+1.3\permil$ VPDB). For many of these previously published studies limited facies descriptions exist which makes it difficult to establish whether this difference can be attributed to the style of tufa formation. However, the fact that the difference in $\delta^{13}C$ values is so consistently different implies that a regional, rather than site specific, control is more likely. Crombie et al. (1997) interpret the -3.3 to $-1.1\permil$ range in $\delta^{13}C$ at Dungul and Dineigel Oases as consistent with the underlying limestone bedrock geology. The isotopically heavier $\delta^{13}C$ from the Kurkur-Dungul area are interpreted by Kele et al. (2021) as reflected evaporative enrichment, as well as rapid degassing and related kinetic effects within an arid climatic setting. At Kharga Oasis Smith et al. (2004) point out that tufa $\delta^{13}C$ is heavy compared to many non-Saharan fossil and modern tufa (generally $< -6\permil$) (e.g. Andrews et al., 1997; Janssen et al., 1999; Arenas et al., 2000; Horvatinčič et al., 2000), and suggest this may be driven by the presence of thin soils (again implying a bedrock-dominated signal), or by a larger percentage of C4 plants in this setting than Europe. C4 vegetation is also raised as a possible driving mechanism by Kieniewicz and Smith (2009) for tufa from the Dakhleh Oases. Here we propose that vegetation and biomass is the most likely cause for the observed difference in $\delta^{13}C$ values. Vegetation can influence the $\delta^{13}C$ value of tufas in two ways. Firstly, the density of vegetation cover and the maturity of soil development can have a strong control on the supply of plant

derived CO_2 to vadose water during recharge (Andrews et al., 1997). As soil respired CO_2 has more a negative $\delta^{13}C$ value than atmospheric CO_2 landscapes with higher biomass and more mature soil profiles are likely to generate tufas with more negative $\delta^{13}C$ values (see Andrews et al., 1997). The type of vegetation can also play key role in $\delta^{13}C$ values in freshwater/pedogenic carbonates with plants that utilise the C3 photosynthetic pathway respiring CO_2 with significantly more negative isotopic values than CO_2 respired by plants that utilise the C4 photosynthetic pathway (Cerling and Quade, 1993).

$\delta^{13}C$ values of -8.4 to -9.6‰ VDP for tufa at Bet Shean (dated to between 20 and 41 ka) overlap with the $\delta^{13}C$ values at Wadi Dabsa (Fig. 3A), and Kroon et al. (1998) interpreted these as indicating precipitation of carbonate from groundwater without any significant evaporation. The other overlapping data are from tufa labelled by Hamdan and Brook (2015) as 'Late Pleistocene' ($\sim$20.4–28.4 cal kyr B. P.), at Wadi Watier ($\sim$7.7‰ VPDB) in the Sinai (Fig. 3A). These isotopically lighter $\delta^{13}C$ values are discussed by Hamdan and Brook (2015), who highlight that the signatures at Wadi Watier are distinct from heavier values at other sites in the eastern desert of Egypt, particularly those dated to the Holocene. They suggest the former may have been driven by higher partial pressures of CO_2 in the soil, alongside reduced evaporation in a more humid, cooler climate in the Late Pleistocene as compared to the Holocene.

In general, the $\delta^{13}C$ value of the Wadi Dabsa samples are typical of those formed under a C3 dominated vegetation, which have not experienced substantial evaporative enrichment (noting the covariation in $\delta^{13}C$ and $\delta^{18}O$ (Fig. 3A) may indicate some enrichment), whilst the isotopically heavier group of tufa within northern Africa may have been influenced by some combination of C4 dominated vegetation, thin soils, and evaporative enrichment. Whilst it is difficult to quantify the contribution of C3:C4 vegetation during different periods of tufa development, it is possible that biomass and vegetation drive differences in $\delta^{13}C$. That the Wadi Dabsa tufas formed under a dense biomass and a landscape characterised by mature soil profiles is consistent with the coastal setting of this site which, at the present day, makes it one of the wettest localities on the Arabian Peninsula.

5.4. Implications of west coast MIS 7 and MIS 5 humid phases for hominin migrations

Intensive, fruitful debates about the dispersal of hominins in the Late Pleistocene are driven by the discovery of lithic assemblages that have led to the revision of dispersal models (e.g. Armitage et al., 2011), and by new hominin fossil finds that are at the heart of these revisions (e.g. Groucutt et al., 2018). There is now a strong body of evidence from the interior of Saudi Arabia for greener landscapes and associated lacustrine conditions. This is perhaps best evidenced in the north of the interior for the Nefud (Petit-Maire et al., 2010; Petraglia et al., 2012; Rosenberg et al., 2013; Jennings et al., 2015; Clark-Balzan et al., 2018; Groucutt et al., 2018; Parton et al., 2018; Groucutt et al., 2021), with a lower spatial density of sites in the south in the Rub' al Khali (Rosenberg et al., 2011; Matter et al., 2015). These were mostly likely 'green corridors', rather than full landscape greening, as discussed in individual papers and raised in key overview papers about hominin migration in this region (e.g. Petraglia et al., 2012; Parton et al., 2015; Timmerman and Friedrich, 2016; Bae et al., 2017). Amongst these records for the interior, there is support for a MIS 7 and MIS 5e humid phase, and perhaps late MIS 6 to 5e transition in places, and also a more persistent MIS 6 humidity in some sites (Fig. 4). Nicholson et al. (2021) highlight the importance of this most intense humid period at MIS 5e within the story of human dispersal and remind us that the presence of the later, and less-intense humid phases, will also hold importance. We can add here, for the first time, a similar palaeoenvironmental history of humid phases during MIS 7 and MIS 6/5e and later parts of MIS 5 on the western coast of Saudi Arabia, west of the Asir Mountains, down on the coastal plain adjacent to the Red Sea. There is therefore, a strong reason to believe the

timing in water resource availability is consistent in the west in the volcanic harrats with other parts of the peninsula. Furthermore, the chemical composition of the tufa indicates this would have been fresh, potable water. This keeps the debate about varied hominin dispersal routes across, and within, Arabia open.

6. Conclusions

Our tufa record at Wadi Dabsa shows for the first time that the southwest coast of Arabia has a similar history of humid phases to those from southern Arabian speleothems and to lacustrine records from the Nefud in the northern interior of Saudi Arabia. This is reflected not only in the broad timing (MIS 7 and MIS 5) but in the apparent magnitude of humidity experienced across these events. MIS 5e has the most negative $\delta^{18}O$, suggesting it was the most humid phase of middle-late Pleistocene. This pattern is supported by climate model simulations for MIS 5e of increased summer precipitation amounts and the spatial pattern in an isotope-enabled climate model simulation, showing more depleted $\delta^{18}O$ across southwest Arabia, as well as the northwest of the horn of Africa and through to central north Africa. The $\delta^{13}C$ signatures of Wadi Dabsa tufa indicate these are cool-water tufa (meteogene) as opposed to thermally-influenced travertine, and are in the typical range for tufa formed under C3 dominated vegetation and without a strong evaporative enrichment effect. $\delta^{13}C$ signatures at Wadi Dabsa differ from signatures for tufa across the Western Desert of Egypt, which may have experienced some combination of C4 dominated vegetation, low biomass and thin soils, and greater evaporative enrichment. In contrast, Wadi Dabsa may have experienced comparatively higher biomass, thicker soils, and wetter conditions with lower evaporative losses.

Our compilation of speleothem, lacustrine and tufa records on the Arabian Peninsula (including Levant and Sinai) and eastern north Africa, indicates some humidity during MIS 6. Thresholds of precipitation for activation of surface hydrological systems may be lower than that required for groundwater recharge, the latter of which drives speleothem growth in southern Arabia. An early MIS 6 timing is currently only recorded north of 23°N, and this spatial pattern requires further testing, via targeting records from the south with deeper stratigraphy and exploring whether the northern region is governed by a different climatic circulation pattern from that in the south. Beyond the Saharo-Arabian belt there is a striking similarity in the timing of humid intervals, indicated by the deposition of tufa and lacustrine carbonates in Europe, including sites in Greece, Croatia, France and Spain. This is occurring in MIS 11, 7 and 5, and also during early MIS 6 (in Croatia, Greece and northeast Spain).

It remains difficult to make conclusive statements about the role of different rainfall regimes across the Saharo-Arabian belt (and further north into Europe) between MIS 6 and interglacials, and across space during the same interval. In part, this is due to a lack of chronological control for much of the available $\delta^{18}O$ freshwater carbonate data. Furthermore, the controls on freshwater carbonate $\delta^{18}O$ are driven by more than solely rainfall source region, reflecting rainfall amount and intensity effects and also any modifications to the water at the (sub) surface, as well as the temperature at which carbonates mineralise. Explorations of the spatial and temporal trends in palaeoclimatic circulation patterns will be improved by increasing numbers of samples with coupled U–Th dates and stable isotopic compositions, continued developments in clumped stable isotopic analysis and speleothem fluid inclusion analysis, and further climatic model simulations.

This study demonstrates that tufa within the volcanic harrats of western Saudi Arabia are a powerful palaeoenvironmental and palaeoclimatic proxy in this region, through parallel measurements of their U–Th chronologies over their growth intervals, coupled to stable isotopic composition. This is supported by the stratigraphical, petrographical and geochemical analysis of these tufa by Stone et al. (2022). This site on the western coast of the Arabian Peninsula is part of a rich record of hominin occupation and dispersal in this region, and the

timing of tufa formation here is part of the growing story of humid windows of opportunity for hominin dispersals during the Late Quaternary.

Author contributions

Declaration of competing interest

The authors declare that they have no known competing financial interests or personal relationships that could have appeared to influence the work reported in this paper.

Data availability

data is in Table 2 and additional data in the the Supp Info files

Acknowledgements

Appendix A. Supplementary data

Supplementary data to this article can be found online at https://doi.org/10.1016/j.quascirev.2023.108333.

References

Abotalib, Z.A., Sultan, M., Elkadiri, R., 2016. Groundwater processes in Saharan Africa: implication for landscape evolution in arid environments. Earth Sci. Rev. 156, 108–136. https://doi.org/10.1016/j.earscirev.2016.03.004.

Abotalib, Z.A., Sultan, M., Jimenez, G., Crossey, L., Karlstrom, K., Krishnamurthy, R.V., Elkadiri, R., Polyak, V., 2019. Complexity of Saharan paleoclimate reconstruction and implications for modern human migration. Earth Planet Sci. Lett. 508, 74–84. https://doi.org/10.1016/j.epsl.2018.12.015.

Andrews, J.E., 2006. Palaeoclimatic records from stable isotopes in riverine tufas: synthesis and review. Earth Sci. Rev. 75, 85–104. https://doi.org/10.1016/j.earscirev.2005.08.002.

Andrews, J.E., Riding, R., Dennis, P.F., 1997. The stable isotope record of environmental and climatic signals in modern terrestrial microbial carbonates from Europe. Palaeogeogr. Palaeoclimatol. Palaeoecol. 129 (1–2), 171–189. https://doi.org/10.1016/S0031-0182(96)00120-4.

Antoine, P., Limondin-Lozouet, N., Auguste, P., Agnés, L., Bahain, J.-J., Falguéres, C., Michel, L., Paule, C., Locht, J.-L., Pascal, D., Fagnar, J.-P., Michel, H., Hátte, C., Mercier, N., Frechen, M., Moigne, A.-M., Munaut, A.-V., Ponel, P., Rousseau, D.-D., 2003. Paléoenvironnements pléistocènes et peuplements paléolithiques dans le bassin de la Somme (nord de la France). n°1, 2003 Bulletin de la Société préhistorique française, tome 100, 5-28.

Antoine, P., Limondin-Lozouet, N., Auguste, P., Locht, J.-L., Galheb, B., Reyss, J.-L., Escudé, E., Carbonel, P., Mercier, N., Bahain, J.-J., Falguéres, C., Voinchet, P., 2006. Le tuf de Caours (Somme, France): mise en évidence d'une séquence eemienne et d'un site paléolithique associé. Quaternair 17 (4), 281–320. https://doi.org/10.4000/quaternaire.880.

Arenas, C., Gutiérrez, F., Osácar, C., Sancho, C., 2000. Sedimentology and geochemistry of fluvio-lacustrine tufa deposits controlled by evaporite solution subsidence in the central Ebro Depression, NE Spain. Sedimentology 47, 883–909.

Arenas-Abad, C., Vázquez-Urbex, M., Pardo-Tirapu, G., Marcén, C., 2010. Fluvial and associated carbonate deposits. In: Alonzo-Zarza, A.M., Tanner, L.H. (Eds.), Carbonates in Continental Settings: Facies, Environments and Processes, Developments in Sedimentology, vol. 61, pp. 133–175.

Armitage, S.J., Jasim, S.A., Marks, A.E., Parker, A.G., Usik, V.I., Uerpmann, H.-P., 2011. The southern route "Out of Africa": evidence for an early expansion of modern humans into Arabia. Science 331, 453–456. https://doi.org/10.1126/science.1199113.

Ayalon, A., Bar-Matthews, M., Kaufman, A., 2002. Climatic conditions during marine isotopic stage 6 in the Eastern Mediterranean region as evident from the isotopic composition of speleothems: Soreq Cave, Israel. Geology 30, 303–306. https://doi.org/10.1130/0091-7613(2002)030%3C0303:CCDMOI%3E2.0.CO;2.

Bae, C.J., Douka, K., Petraglia, M.D., 2017. On the origin of modern humans: asian perspectives. Science 358 (6368), eaai9067. https://doi.org/10.1126/science.aai9067.

Bailey, G.N., 2009. The Red Sea, coastal landscapes, and hominin dispersals. In: Petraglia, M.D., Rose, J.I. (Eds.), The Evolution of Human Populations in Arabia. Springer, Amsterdam, pp. 15–37. https://doi.org/10.1007/978-90-481-2719-1_2.

Bailey, G.N., Deves, M.H., Inglis, R.H., Meredith-Williams, M.G., Momber, G., Sakellariou, D., Sinclair, A.G.M., Rousakis, G., Al Ghamdi, S., Alsharekh, A.M., 2015. Blue Arabia: Palaeolithic and underwater survey in SW Saudi Arabia and the role of coasts in Pleistocene dispersals. Quat. Int. 382, 42–57. https://doi.org/10.1016/j.quaint.2015.01.002.

Bar-Matthews, M., Ayalon, A., 2004. Speleothems as palaeoclimate indicators, a case study from Soreq Cave, located in the eastern Mediterranean region, Israel. In: Batterbee, R.W. (Ed.), Past Climate Variability through Europe and Africa. Kluwer Academic Publishers, Dordrecht, The Netherlands, pp. 363–391. https://link.springer.com/chapter/10.1007/978-1-4020-2121-3_18.

Bar-Matthews, M., Ayalon, A., Kaufman, A., 1997. Late Quaternary paleoclimate in the eastern Mediterranean region from stable isotope analysis of speleothems at Soreq Cave, Israel. Quat. Res. 47, 155–168. https://doi.org/10.1006/qres.1997.1883.

Bar-Matthews, M., Ayalon, A., Gilmour, M., Matthews, A., Hawkesworth, C.J., 2003. Sea-land oxygen isotopic relationships from planktonic foraminifera and speleothems in the Eastern Mediterranean region and their implication for paleorainfall during interglacial intervals. Geochim. Cosmochim. Acta 67 (17), 3181–3199. https://doi.org/10.1016/S0016-7037(02)01031-1.

Black, E., 2011. The influence of the North Atlantic Oscillation and European circulation regimes on the daily to interannual variability of winter precipitation in Israel. Int. J. Clim. 32, 1654–1664. https://doi.org/10.1002/joc.2383.

Brasier, A.T., Andrews, J.E., Kendall, A.C., 2011. Diagenis or dire genesis? The origin of columnar spar in tufa stromatolites of central Greece and the role of chironomid

larvae. Sedimentology 58 (5), 1283–1302. https://doi.org/10.1111/j.1365-3091.2010.01208.x.

Breeze, P.S., Groucutt, H.S., Drake, N.A., White, T.S., Jennings, R.P., Petraglia, M.D., 2016. Palaeohydrological corridors for hominin dispersals in the Middle East ~250-70,000 years ago. Quat. Sci. Rev. 144, 155–185. https://doi.org/10.1016/j.quascirev.2016.05.012.

Brook, G., Embabi, N., Ashour, M.M., Edwards, R., Cheng, H., Cowart, J., Dabous, A., 2002. Djara cave in the Western Desert of Egypt: morphology and evidence of quaternary climatic change. Cave Karst Sci. 29 (2), 57–66.

Brookes, I.A., 2010. Spatially variable sedimentary responses to orbitally driven pluvial climate during Marine Oxygen Isotope Stage 5.1, Dakhla Oasis region, Egypt. Quat. Res. 74, 252–264. https://doi.org/10.1016/j.yqres.2010.05.001.

Burns, S.J., Fleitmann, D., Matter, A., Neff, U., Mangini, A., 2001. Speleothem evidence from Oman for continental pluvial events during interglacial periods. Geology 29, 623–626. https://doi.org/10.1130/0091-7613(2001)029%3C0623:SEFOFC%3E2.0.CO;2.

Candy, I., Adamson, K., Gallant, C.E., Whitfield, E., Pope, R., 2012. Oxygen and carbon isotopic composition of Quaternary meteoric carbonates from western and southern Europe: their role in palaeoenvironmental reconstruction. Palaeogeogr. Palaeoclimatol. Palaeoecol. 326–328, 1–11. https://doi.org/10.1016/j.palaeo.2011.12.017.

Capezzouli, E., Gandin, A., Pedley, M., 2014. Decoding tufa and travertine (fresh water carbonates) in the sedimentary record: the state of the art. Sedimentology 61, 1–21. https://doi.org/10.1111/sed.12075.

Cerling, T.E., Quade, J., 1993. Stable Carbon and Oxygen Isotopes in Soil Carbonates, vol. 78. American Geophysical Union Geophysical Monograph Series, Washington DC, pp. 217–231.

Clark-Balzan, L., Parton, A., Breeze, P.A., Groucutt, H.S., Petrglia, M.D., 2018. Resolving problematic luminescence chronologies for carbonate-and evaporite-rich sediments spanning multiple humid periods in the Jubbah Basin, Saudi Arabia. Quat. Geochron. 45, 50–73. https://doi.org/10.1016/j.quageo.2017.06.002.

Crassard, R., Hilbert, Y.H., 2013. A Nubian complex site from Central Arabia: implications for Levallois taxonomy and human dispersals during the upper Pleistocene. PLoS One 8, e69221. https://doi.org/10.1371/journal.pone.0069221.

Crassard, R., Hilbert, Y.H., Preusser, F., Wulf, G., Schiettecatte, J., 2019. Middle Palaeolithic occupations in central Saudi Arabia during MIS 5 and MIS 7: new insights on the origins of the peopling of Arabia. Archaeol. Anthropol. Sci. 11, 3101–3120.

Cremaschi, M., Zerboni, A., Spötl, C., Felletti, F., 2010. The calcareous tufa in the Tadrart Acacus Mt. (SW Fezzan, Libya) an early Holocene palaeoclimate archive in the central Sahara. Palaeogeogr. Palaeoclimatol. Palaeoecol. 81, 81–94. https://doi.org/10.1016/j.palaeo.2010.01.019.

Crombie, M.K., Arvidson, R.E., Sturchio, N.C., Alfy El, Z., Zeid, K.A., 1997. Age and isotopic constraints on Pleistocene pluvial episodes in the Western Desert, Egypt. Palaeogeogr. Palaeoclimatol. Palaeoecol. 130 (1), 337–355. https://doi.org/10.1016/S0031-0182(96)00134-4.

Dabkowski, J., Limondin-Lozouet, N., Antoine, P., Andrews, J., Marca-Bell, A., Robert, V., 2012. Climatic variations in MIS 11 recorded by stable isotopes and trace elements in a French tufa (La Celle, Seine Valley. J. Quat. Sci. 27 (8), 790–799. https://doi.org/10.1002/jqs.2567.

Dabkowski, J., Andrews, J., Antoine, P., Marca-Bell, A., 2013. Stable isotope record of Eemian seasonal temperature from MIS 5e tufa stromatolite. Somme Basin, Northern France. Clim. Past Discussi. 9 (2), 1657–1674. https://doi.org/10.5194/cpd-9-1657-2013.

de Vries, A.J., Tyrlis, E., Edry, D., Krichak, S.O., Steil, B., Lelieveld, J., 2013. Extreme precipitation events in the Middle East: dynamics of the active Red Sea Trough. JGR Atmos 118 (13), 7087–7710. https://doi.org/10.1002/jgrd.50569, 8.

Drake, N.A., Blench, R.M., Armitage, S.J., Bristow, C.S., White, K.H., 2011. Ancient watercourses and biogeography of the Sahara explain the peopling of the desert. Proc. Natl. Acad. Sci. 108, 458–462. https://doi.org/10.1073/pnas.1012231108.

Drake, N., Breeze, P., Parker, A., 2013. Palaeoclimate in the saharan and arabian deserts during the middle palaeolithic and the potential for hominin dispersals. Quat. Int. 300, 48–61. https://doi.org/10.1016/j.quaint.2012.12.018.

El-Shenawy, M.I., Kim, S.-T., Schwarcz, H.P., Asmerom, Y., Polyak, V.J., 2018. Speleothem evidence for the greening of the Sahara and its implications for the early human dispersal out of sub-Saharan Africa. Quat. Sci. Rev. 188, 67–76. https://doi.org/10.1016/j.quascirev.2018.03.016.

Farrant, A.R., Ellison, R.A., Thomas, B., Pharaoh, T.C., Newell, B., Goodenough, K.M., Lee, J.R., Know, R.W., 2012. The geology and geophysics of the United Arab Emirates. Volume 6. In: Geology of the Western and Central United Arab Emirates. British Geological Survey, Keyworth, Nottingham, p. 371.

Findlater, J., 1969. A major low level air current near the Indian Ocean during the northern summer. Q. J. R. Meteorol. Soc. 95, 362–380. https://doi.org/10.1002/qj.49709540409.

Fleitmann, D., Burns, S.J., Mudelsee, M., Neff, U., Kramers, J., Mangini, A., Matter, A., 2003a. Holocene forcing of the Indian monsoon recorded in a stalagmite from Southern Oman. Science 300, 737–1739. https://doi.org/10.1126/science.1083130.

Fleitmann, D., Burns, S.J., Neff, U., Mangini, A., Matter, A., 2003b. Changing moisture sources over the last 330,000 years in Northern Oman from fluid-inclusion evidence in speleothems. Quat. Res. 60 (2), 223–232. https://doi.org/10.1016/S0033-5894(03)00086-3.

Fleitmann, D., Burns, S.J., Mangini, A., Mudelsee, M., Kramers, J., Villa, I., Neff, U., Al-Subbary, A.A., Buettner, A., Hippler, D., Matter, A., 2007. Holocene ITCZ and Indian monsoon dynamics recorded in stalagmites from Oman and Yemen (Socotra). Quat. Sci. Rev. 26, 170–188. https://doi.org/10.1016/j.quascirev.2006.04.012.

Fleitmann, D., Burns, S.J., Pekala, M., Mangini, A., Al-Subbary, A., Al-Aowah, M., Kramers, J., Matter, A., 2011. Holocene and Pleistocene pluvial periods in Yemen, southern Arabia. Quat. Sci. Rev. 30, 783–787. https://doi.org/10.1016/j.quascirev.2011.01.004.

Ford, T.D., Pedley, H.M., 1996. A review of tufa and travertine deposits of the world. Earth Sci. Rev. 41, 117–175. https://doi.org/10.1016/S0012-8252(96)00030-X.

Foulds, W.F., Shuttleworth, A., Sinclair, A., Alsharekh, A.M., Al Ghamdi, S., Inglis, R.H., Bailey, G.N., 2017. A large handaxe from Wadi Dabsa and early hominin adaptations within the Arabian Peninsula. Antiquity 91 (360), 1421–1434. https://doi.org/10.15184/aqy.2017.153.

Garnett, E.R., Gilmour, M.A., Rowe, P.J., Andrews, J.E., Preece, R.C., 2004. Quat. Sci. Rev. 23 (7–8), 947–958. https://doi.org/10.1016/j.quascirev.2003.06.018.

GEBCO Compilation Group, 2022. GEBCO_2022 Grid. https://doi.org/10.5285/e0f0bb80-ab44-2739-e053-6c86abc0289c.

Gierz, P., Werner, M., Lohmann, G., 2017. Simulating climate and stable water isotopes during the Last Interglacial using a coupled climate-isotope model. J. Adv. Model. Earth Syst. 9, 2027–2045. https://doi.org/10.1002/2017MS001056.

Grant, K.M., Rohling, E.J., 2014. Sea-level variability over five glacial cycles. et al. Nat. Commun. 5076 https://doi.org/10.1038/ncomms6076.

Grant, K.M., Rohling, E.J., Westerhold, T., Zabel, M., Heslop, D., Konijnendijk, T., Lourens, L., 2017. A 3 million year index for North African humidity/aridity and the implication of potential pan-African Humid periods. Quat. Sci. Rev. 171, 100–118. https://doi.org/10.1016/j.quascirev.2017.07.005.

Groucutt, H.S., Petraglia, M.D., Bailey, G., Scerri, E.M.L.L., Parton, A., Clark-Balzan, L., Jennings, R.P., Lewis, L., Blinkhorn, J., Drake, N.A., Breeze, P.S., Inglis, R.H., Deves, M.H., Meredith-Williams, M., Boivin, N., Thomas, M.G., Scally, A., Deves, M.H., Meredith-Williams, M., Boivin, N., Thomas, M.G., Scally, A., 2015. Rethinking the dispersal of Homo sapiens out of Africa. Evol. Anthropol. 24, 149–164. https://doi.org/10.1002/evan.21455.

Groucutt, H.S., Grün, R., Zalmout, I.A.S., Drake, N.A., Armitage, S.J., Candy, I., Clark-Wilson, R., Louys, J., Breeze, P.S., Duval, M., Buck, L.T., Kivell, T.L., Pomeroy, E., Stephens, N.B., Stock, J.T., Stewart, M., Price, G.J., Kinsley, L., Sung, W.W., Alsharekh, A., Al-Omari, A., Zahir, M., Memesh, A.M., Abdulshakoor, A.J., Al-Masari, A.M., Bahameem, A.A., Al Murayyi, K.M.S., Zahrani, B., Scerri, E.L.M., Petraglia, M.D., Gramp, R., S Zalmout, I.A., Drake, N.A., Armitage, S.J., Candy, I., Clark-Wilson, R., Louys, J., Breeze, P.S., Duval, M., Buck, L.T., Kivell, T.L., Pomeroy, E., Stephens, N.B., Stock, J.T., Stewart, M., Price, G.J., Kinsley, L., Wai Sung, W., Alsharekh, A., Al-Omari, A., Zahir, M., Memesh, A.M., Abdulshakoor, A.J., Al-Masari, A.M., Bahameem, A.A., S Al Murayyi, K.M., Zahrani, B., M Scerri, E.L., Petraglia, M.D., 2018. Homo sapiens in Arabia by 85,000 years ago. Nat. Ecol. Evol. 2, 800–809. https://doi.org/10.1038/s41559-018-0518-2.

Groucutt, H.S., White, T.S., Scerri, E.M.L., Andrieux, E., Clark-Wilson, R., Breeze, P.S., Armitage, S.J., Stewart, M., Drake, N., Louys, J., Price, G.J., Duval, M., Parton, A., Candy, I., Carleton, W.C., Shipton, C., Jennings, R.P., Zahir, M., Blinkhorn, J., Blockley, S., Al-Omari, A., Alsharekh, A.M., Petraglia, M.D., 2021. Multiple hominin dispersals into Southwest Asia over the past 400,000 years. Nature 597, 376–380. https://doi.org/10.1038/s41586-021-03863-y.

Hamdan, M.A., Brook, G.A., 2015. Timing and characteristics of Late Pleistocene and Holocene wetter periods in the Eastern Desert and Sinai of Egypt, based on 14C dating and stable isotope analysis of spring tufa deposits. Quat. Sci. Rev. 130, 168–188. https://doi.org/10.1016/j.quascirev.2015.09.011.

Hasanean, H., Almazroui, M., 2015. Rainfall: features and variations over Saudi Arabia, A review. Climate 3, 578–626. https://doi.org/10.3390/cli3030578.

Hays, P.D., Grossman, E.L., 1991. Oxygen isotopes in meteoric calcite cements as indicators of continental paleoclimate. Geology 19, 441–444. https://doi.org/10.1130/0091-7613(1991)019%3C0441:OIIMCC%3E2.3.CO;2.

Hellstrom, J., 2006. U-Th dating of speleothems with high initial ^{230}Th using stratigraphical constraint. Quat. Geochron. 1 (4), 289–295. https://doi.org/10.1016/j.quageo.2007.01.004.

Herold, M., Lohmann, G., 2009. Eemian tropical and subtropical African moisture transport: an isotope modelling study. Clim. Dyn. 33, 1075–1088. https://doi.org/10.1007/s00382-008-0515-2.

Hoffmann, G., Rupprechter, M., Rahn, M., Preusser, F., 2015. Fluvio-Lacustrine deposits reveal precipitation pattern in SE Arabia during early MIS 3. Quat. Int. 382, 145–153. https://doi.org/10.1016/j.quaint.2014.10.053.

Hoffmann, G., Rogerson, M., Spötl, C., Luetscher, M., Vance, D., Osborne, A.H., Fello, N.M., Moseley, G.E., 2016. Timing and causes of North African wet phases during the last glacial period and implications for modern human migration. Sci. Rep. 6, 36367 https://doi.org/10.1038/srep36367.

Horvatinčič, N., Čalić, R., Geyh, M.A., 2000. Interglacial growth of tufa in Croatia. Quat. Res. 53, 185–195.

Inglis, R.H., Fanning, P.C., Stone, A., Barfod, D.N., Sinclair, A., Chang, H.-S., Alsjarekh, A.M., Bailey, G., 2019. Palaeolithic artifact deposits at Wadi Dabsa, Saudi Arabia: a multiscalar geoarchaeological approach to building an interpretative framework. Geoarchaeology 34 (3), 272–294. https://doi.org/10.1002/gea.21723.

Janssen, A., Swennen, R., Podoor, N., Keppens, E., 1999. Biological and diagenetic influences in Recent and fossil tufa deposits from Belgium. Sed. Geol. 126, 75–95.

Jennings, R.P., Singarayer, J., Stone, E.J., Krebs-Kanzow, U., Khon, V., Nisancioglu, K.H., Pfeiffer, M., Zhang, X., Parker, A., Parton, A., Groucutt, H.S., White, T.S., Drake, N.A., Petraglia, M.D., 2015. The greening of Arabia: multiple opportunities for human occupation of the Arabian Peninsula during the Late Pleistocene inferred from an ensemble of climate model simulations. Quat. Int. 382, 181–199. https://doi.org/10.1016/j.quaint.2015.01.006.

Jimenez, G., 2014. Travertine from Egypt's Western Desert: A Terrestrial Record of North African Paleohydrology and Paleoclimate during the Late Pleistocene. MSc thesis, University of New Mexico, Albuquerque, USA.

Kabesh, M.M.L., Abdel-Motelib, A., 2014. Quaternary tufa profiles, jabal faransan-wadi qedid area, southern Saudi Arabia. Geopolit. Hist. Int. Relat. 6 (1), 146–159.

Kele, S., Sallam, E.S., Capezzuoli, A., Rogerson, M., Wanas, H., Shen, C.-C., Lone, M.A., Yu, T.-L., Schauer, A., Huntington, K.W., 2021. Were springline carbonates in the Kurkur–Dungul area (southern Egypt) deposited during glacial periods? J. Geol. Soc. London 178, jgs2020–j2147. https://doi.org/10.1144/jgs2020-147.

Kieniewicz, J.M., Smith, J.R., 2009. Palaeoenvironmental reconstruction and water balance of a mid-Pleistocene pluvial lake, Dakleh Oasis, Egypt. Geol. Soc. Am. Bull. 121 (7–8), 1154–1171. https://doi.org/10.1130/B26301.1.

Khalaf, F.I., 2017. Occurrence and genesis of quaternary microbialitic tufa at hammam Al ali, Oman. J. Afr. Earth Sci. 129, 417–426. https://doi.org/10.1016/j.jafrearsci.2017.01.032.

Kim, S.T., O'Neil, J.R., 1997. Equilibrium and non-equilibrium oxygen isotope effects in synthetic carbonates. Geochim. Cosmochim. Acta 61, 3461–3475. https://doi.org/10.1016/S0016-7037(97)00169-5.

Kleindienst, M.R., Schwarcz, H.P., Nicoll, K.A., Churcher, C.S., Frizano, J., Giegengack, R., Wiseman, M.F., 2008. Water in the Desert: First Report on Uranium series Dating of Caton-Thompson's and Gardner's 'Classic' Pleistocene Sequence at Refuf Pass, Kharga Oasis. In: Wiseman, M.F. (Ed.), The Oasis Papers 2. Proceedings of the Second International Conference of the Dakhleh Oasis Project. Oxbow Books, Oxford, pp. 25–54.

Kleindienst, M., Smith, J.R., Adelsberger, K.A., 2009. The Kharga oasis prehistory project (KOPP), 2008 field season: PART I. Geoarchaeology and Pleistocene prehistory. Nyame Akuma 71, 18–30.

Krishnamurti, T.N., Bhalme, H.N., 1976. Oscillation of a monsoon system, Part I: observational aspects. J. Atmos. Sci. 33, 1937–1954. https://doi.org/10.1175/1520-0469(1976)033%3C1937:OOAMSP%3E2.0.CO;2.

Kronfeld, J., Vogel, J.C., Rosenthal, E., Weinstinevron, M., 1988. Age and Paleoclimatic Implications of the Bet Shean Travertines. Quat. Res. 30 (3), 298–303. https://doi.org/10.1016/0033-5894(88)90005-1.

Kroon, D., Alexander, I., Little, M., Lourens, L.J., Matthewson, A., Roberston, A.H.F., Sakamoto, T., 1998. Oxygen isotope and sapropel stratigraphy in the eastern Mediterranean during the last 3.2 million years. In: Robertson, A.H.F., Emeis, K.-C., Richter, C., Camerlenghi, A. (Eds.), Proceedings of the Ocean Drilling Program, Scientific Results, vol. 160, pp. 181–189.

Kutzbach, J.E., 1981. Monsoon climate of the early Holocene: climate experiment with the earth's orbital parameters for 9000 Years ago. Science 214 (4516), 59–61. https://doi.org/10.1126/science.214.4516.59.

Kutzbach, J.E., Guan, J., He, F., Cohen, A.S., Orland, I.J., Chen, G., 2020. African climate response to orbital and glacial forcing in 140,000-y simulation with implications for early modern human environments. Proc. Natl. Acad. Sci. USA 117 (5), 2255–2264. https://doi.org/10.1073/pnas.1917673117.

Larrasoaña, J.C., Roberts, A.P., Rohling, E.J., 2013. Dynamics of green Sahara periods and their role in hominin evolution. PLoS One 8 (10), e76514. https://doi.org/10.1371/journal.pone.0076514.

Lisiecki, L.E., Raymo, M.E., 2005. A Pliocene-Pleistocene stack of 57 globally distributed benthic δ18O records. Paleoceanography 20, PA1003. https://doi.org/10.1029/2004PA001071.

Matter, A., Neubert, E., Preusser, F., Rosenberg, T., 2015. Palaeo-environmental implications derived from lake and sabkha deposits of the southern Rub' al-Khali, Saudi Arabia and Oman. Quat. Int. 382, 120–131. https://doi.org/10.1016/j.quaint.2014.12.029.

McLaren, S.J., Al-Juaidi, F., Bateman, M.D., Millington, A.C., 2009. First evidence for episodic flooding events in the arid interior of central Saudi Arabia over the last 60 ka. J. Quat. Sci. 24, 198–207. https://doi.org/10.1002/jqs.1199.

Nicholson, S.L., Jacobson, M.J., Hosfield, R., Fleitmann, D., 2021. The stalagmite record of southern Arabia: climatic extremes, human evolution and societal development. Front. Earth Sci. 9, 749488 https://doi.org/10.3389/feart.2021.749488.

Nicholson, S.L., Pike, A.W.G., Hosfield, R., Roberts, N., Sahy, D., Woodhead, J., Cheng, H., Edwards, R.L., Affolter, S., Leuenberger, M., Burns, S.J., Matter, A., Fleitmann, D., 2020. Pluvial periods in Southern Arabia over the last 1.1 million-years. Quat. Sci. Rev. 229, 106112 https://doi.org/10.1016/j.quascirev.2019.106112.

Ohishi, M., Sugimoto, S., Hanawa, K., 2015. Zonal movement of the Mascarene High in austral summer. Clim. Dyn. 45, 1739–1745. https://doi.org/10.1007/s00382-014-2427-7.

Oritz, J.E., Torres, T., Delgado, A., Reyes, E., Díaz-Bautista, A., 2009. A review of the Tagus river tufa deposits (central Spain): age and palaeoenvironmental record. Quat. Sci. Rev. 28, 947–996.

Otto-Bliesner, B.L., Marshall, S.J., Overpeck, J.T., Miller, G.H., Hu, A., 2006. Simulating arctic climate warmth and icefield retreat in the last interglaciation. Science 311, 1751–1753. https://doi.org/10.1126/science.1120808.

Parton, A., Clark-Balzan, L., Parker, A.G., Preston, G.W., Sung, W.W., Breeze, P.S., Leng, M.J., Groucutt, H.S., White, T.S., Alsharekh, A., Petraglia, M.D., 2018. Middle-late quaternary palaeoclimate variability from lake and wetland deposits in the Nefud Desert, northern Arabia. Quat. Sci. Rev. 202, 78–97. https://doi.org/10.1016/j.quascirev.2018.10.010.

Parton, A., White, T.S., Parker, A.G., Breeze, P.S., Jennings, R., Groucutt, H.S., Petraglia, M.D., 2015. Orbital-scale climate variability in Arabia as a potential motor for human dispersals. Quat. Int. 382, 82–97. https://doi.org/10.1016/j.quaint.2015.01.005.

Petit-Maire, N., Carbonel, P., Reyss, J.L., Sanlaville, P., Abed, A., Bourrouilh, R., Fontugne, M., Yasin, S., 2010. A vast Eemian palaeolake in Southern Jordan (29°N). Glob. Planet. Change 57, 9–21. https://doi.org/10.1016/j.gloplacha.2010.01.012.

Petraglia, M.D., 2003. The lower palaeolithic of arabian peninsula: occupations, adaptations, and dispersals. J. World Prehist. 17 (2), 141–179. https://doi.org/10.1023/A:1025849206519.

Petraglia, M.D., Alsharekh, A., Breeze, P., Clarkson, C., Crassard, R., Drake, N.A., Groucutt, H.S., Jennings, R., Parker, A.G., Parton, A., Roberts, R.G., Shipton, C., Matheson, C., al-Omari, A., Veall, M.A., 2012. Hominin dispersal into the Nefud desert and middle Palaeolithic settlement along the Jubbah palaeolake, northern Arabia. PLoS One 7 (11), e49840. https://doi.org/10.1371/journal.pone.0049840.

Roberts, P., Stewart, M., Alagaili, A.N., Breeze, P., Candy, I., Drake, N., Groucutt, H.S., Scerri, E.M.L., Lee-Thorp, J., Louys, J., Zalmout, I.S., Al-Mufarreh, Y.S.A., Zech, J., Alsharekh, A.M., al Omari, A., Boivin, N., Petraglia, M., 2018. Fossil herbivore stable isotopes reveal middle Pleistocene hominin palaeoenvironment in 'Green Arabia'. Nat. Ecol. Evol. 2, 1871–1878. https://doi.org/10.1038/s41559-018-0698-9.

Rodwell, M.J., Hoskins, B.J., 1996. Monsoons and the dynamics of deserts. Q. J. Meteorol. Soc. 122, 1385–1404. https://doi.org/10.1002/qj.49712253408.

Rogerson, M., Dublyansky, Y., Hoffman, D.L., Luetscher, M., Töchterle, P., Spötl, C., 2019. Enhanced Mediterranean water cycle explains increased humidity during MIS 3 in North Africa. Clim. Past 15, 1757–1769. https://doi.org/10.5194/cp-15-1757-2019.

Rohling, E.J., Grant, K.M., Roberts, A.P., Larrasoaña, J.-C., 2013. Palaeoclimate variability in the mediterranean and Red Sea regions during the last 500,000 years: implications for hominin migrations. Curr. Anthropol. 54, S183–S201. https://doi.org/10.1086/673882.

Rohling, E.J., Marino, G., Grant, K.M., 2015. Mediterranean climate and oceanography, and the periodic development of anoxic events (sapropels). Earth Sci. Rev. 143, 62–97. https://doi.org/10.1016/j.earscirev.2015.01.008.

Rosenberg, T.M., Preusser, F., Fleitmann, D., Schwalb, A., Penkman, K., Schmid, T.W., Al-Shanti, M.A., Kadi, K., Matter, A., 2011. Humid periods in southern Arabia: windows of opportunity for modern human dispersal. Geology 39, 1115–1118. https://doi.org/10.1130/G32281.1.

Rosenberg, T.M., Preusser, F., Risberg, J., Plikk, A., Kadi, K.A., Matter, A., Fleitmann, D., 2013. Middle and Late Pleistocene humid periods recorded in palaeolake deposits of the Nafud desert, Saudi Arabia. Quat. Sci. Rev. 70, 109–123. https://doi.org/10.1016/j.quascirev.2013.03.017.

Rowe, P.J., Wickens, L.B., Sahy, D., Marca, A.D., Peckover, E., Noble, S., Özkul, M., Baykara, M.O., Millar, I.L., Andrews, J.E., 2020. Multi-proxy speleothem record of climate instability during the early last interglacial in southern Turkey. Palaeogeogr. Palaeoclimatol. Palaeoecol. 538, 1049422 https://doi.org/10.1016/j.palaeo.2019.109422.

Rozanski, K., Araguás-Araguás, L., Gonfiantini, R., 1992. Relation between long-term trends of Oxygen-18 isotope composition of precipitation and climate. Science 258, 981–985. https://doi.org/10.1126/science.258.5084.981.

Rozanski, K., Araguás-Araguás, L., Gonfiantini, R., 1993. Isotopic patterns in modern global precipitation. In: Climate Change in Continental Isotopic Record, vol. 78. Geophysical Monographs, pp. 1–36. https://doi.org/10.1029/GM078p0001.

Sancho, C., Arena, C., Vázquez-Urbez, M., Pardo, G., Lozana, M., Peña-Monné, J.L., Hellstrom, J., Ortiz, J.E., Osácar, M.C., Auqué, L., Torres, T., 2015. Climatic implications of the Quaternary fluvial tufa record in the NW Iberian Peninsula over the last 500 ka. Quat. Res. 84, 398–414.

Sanderson, D.W., Kinnaird, T.C., 2019. Optically stimulated luminescence dating as a geochronological tool for Late Quaternary sediments in the Red Sea Region. In: Rasul, N.M.A., Stewart, I.C.F. (Eds.), Geological Setting, Palaeoenvironment and Archaeology of the Red Sea. Springer, Switzerland, pp. 685–707. https://doi.org/10.1007/978-3-319-99408-6_31.

Scerri, E.M.L., Shipton, C., Clark-Balzan, L., Frouin, M., Schwenninger, J.-L., Groucutt, H.S., Breeze, P.S., Parton, A., Blinkhorn, J., Drake, N.A., Jennings, R., Cuthbertson, P., Omari, A. Al, Alsharekh, A.M., Petraglia, M.D., 2018. The expansion of later Acheulean hominins into the Arabian Peninsula. Sci. Rep. 8, 17165 https://doi.org/10.1038/s41598-018-35242-5.

Sen, Z., Al-Suba'I, K.A., 2002. Hydrological considerations for dam siting in arid regions: a Saudi Arabian study. Hydrol. Sci.-J.-des Sci. Hydrologiques 47 (2), 173–186. https://doi.org/10.1080/02626660209492922.

Shipton, C., Blinkhorn, J., Breeze, P.S., Cuthbertson, P., Drake, N., Groucutt, H.S., Jennings, R.P., Parton, A., Scerri, E.M.L., Alsharekh, A., Petraglia, M.D., 2018. Acheulean technology and landscape use at Dawadmi, central Arabia. PLoS One 13 (7), e0200497. https://doi.org/10.1371/journal.pone.0200497.

Smith, J.R., Giegengack, R., Schwarcz, H.P., 2004. Constraints on Pleistocene pluvial climates through stable-isotope analysis of fossil-spring tufas and associated gastropods, Kharga Oasis, Egypt. Palaeogeogr. Palaeoclimatol. Palaeoecol. 206 (1–2), 157–175. https://doi.org/10.1016/j.palaeo.2004.01.021.

Smith, J.R., Hawkins, A.L., Asmerom, Y., Polyak, V., Giegengack, R., 2007. New age constraints on the middle Stone age occupations of Kharga oasis. Western Desert, Egypt 52, 690–701. https://doi.org/10.1016/j.jhevol.2007.01.004. J. Hum. Evol.

Stewart, M., Clark-Wilson, R., Breeze, P.S., Janulis, K., Candy, I., Armitage, S.J., Ryves, D.B., Louys, J., Duval, M., Price, G.J., Cutherbertson, P., Bernal, M.A., Drake, N.A., Alsharekh, A.M., Zahrani, B., Al-Omari, A., Roberts, P., Groucutt, H.S., Petraglia, M.D., 2020. Human footprints provide snapshot of last interglacial ecology in the Arabian interior. Sci. Adv. 6, eaba8940 https://doi.org/10.1126/sciadv.aba8940.

Stone, A., Viles, H.A., Thomas, L., van Calsteren, P., 2010. Can 234U-230Th dating be used to date large semi-arid tufas? Challenges from a study in the Naukluft Mountains, Namibia. J. Quat. Sci. 25 (8), 1360–1372. https://doi.org/10.1002/jqs.1435.

Stone, A., Inglis, R., Barfod, D., Ickert, R., Hughes, L., Waters, J., Jouran, A.-L., Alsharekh, A.M., 2022. Hydroclimatic and geochemical palaeoenvironmental records within tufa: a cool-water fluvio-lacustrine tufa system in the Wadi Dabsa

volcanic setting, western Saudi Arabia. Sediment. Geol. 437, 106181 https://doi.org/10.1016/j.sedgeo.2022.106181.

Sultan, M., Sturchio, N., Hassan, F.A., Hamdan, M.A.R., Mahmood, A.M., Alfy, Z.E., Stein, T., 1997. Precipitation source inferred from stable isotopic composition of Pleistocene groundwater and carbonate deposits in the Western desert of Egypt. Quat. Res. 48 (1), 29–37. https://doi.org/10.1006/qres.1997.1907.

Tierney, J.E., deMenocal, P.B., Zander, P.D., 2017. A climatic context for the out-of-Africa migration. Geology 45, 1023–1026. https://doi.org/10.1130/G39457.1.

Timmerman, A., Friedrich, T., 2016. Late Pleistocene climate drivers of early human migration. Nature 538, 92–95. https://doi.org/10.1038/nature19365.

Tyrlis, E., Lelieveld, J., Steil, B., 2013. The summer circulation over the eastern Mediterranean and the Middle East: influence of the South Asian monsoon. Clim. Dyn. 40, 1103–1123. https://doi.org/10.1007/s00382-012-1528-4.

Vaks, A., Bar-Matthews, M., Ayalon, A., Matthews, A., Frunkin, A., Dayan, U., Halicz, L., Almogi-Labin, A., Schilman, B., 2006. Paleoclimate and location of the border between Mediterranean climate region and the Saharo-Arabian Desert as revealed by speleothems from the northern Negev Desert, Israel. Earth Planet Sci. Lett. 249, 384–399. https://doi.org/10.1016/j.epsl.2006.07.009.

Vaks, A., Bar-Matthews, M., Matthews, A., Ayalon, A., Frumkin, A., 2010. Middle-late Quaternary paleoclimate of northern margins of the Saharan-Arabian desert: reconstruction from speleothems of Negev desert, Israel. Quat. Sci. Rev. 29, 2647–2662. https://doi.org/10.1016/j.quascirev.2010.06.014.

Vaks, A., Woodhead, J., Bar-Matthews, M., Ayalon, A., Cliff, R.A., Zilberman, T., Matthews, A., Frumkin, A., 2013. Pliocene-Pleistocene climate of the northern margin of Saharan-Arabian Desert recorded in speleothems from the Negev Desert,

Israel. Earth Planet Sci. Lett. 368, 88–100. https://doi.org/10.1016/j.epsl.2013.02.027.

Viles, H.A., Taylor, M.P., Nicoll, K., Neumann, S., 2007. Facies evidence of hydroclimatic regime shifts in tufa depositional sequences from the arid Naukluft Mountains, Namibia. Sediment. Geol. 195, 39–53. https://doi.org/10.1016/j.sedgeo.2006.07.007.

Wang, P.X., Wang, B., Cheng, H., Fasullo, J., Gui, Z.T., Kiefer, R., Liu, Z.L., 2017. The global monsoon across time scales: mechanisms and outstanding issues. Earth Sci. Rev. 174, 84–121. https://doi.org/10.1016/j.earscirev.2017.07.006.

Whitton, B.A., Khoja, T.M., Arif, I.A., 1986. Water chemistry and algal vegetation of streams in the Asir Mountains, Saudi Arabia. Hydrobiologia 133, 97–106. https://doi.org/10.1007/BF00031859.

Wilson, G.P., Frogley, M.R., Roucoux, K.H., Jones, T.D., Leng, M.J., Lawson, I.T., Hughes, P.D., 2013. Limnetic and terrestrial responses to climate change during the onset of the penultimate glacial stage in NW Greece. Glob. Planet. Change 107, 213–225.

Woor, S., Buckland, C., Parton, A., Thomas, D.S.G., 2022. Assessing the robustness of geochronological records from the Arabian Peninsula: a new synthesis of the last 20 ka. Glob. Planet. Change, 103748. https://doi.org/10.1016/j.gloplacha.2022.103748.

World Clim, 2015. World clim-global climate data: free climate data for ecological modeling and GISVery high resolution interpolated climate surfaces for global land areas. Available at: https://www.worldclim.com/.

Yu, Y., Notaro, M., Kalashnikova, O.V., Garay, M.J., 2016. Climatology of summer Shamal wind in the Middle East. JGR Atmospheres 121 (1), 289–305. https://doi.org/10.1002/2015JD024063.